



**HAL**  
open science

## Three-dimensional gravity anomaly inversion in the Pyrenees using compressional seismic velocity model as structural similarity constraints

Roland Martin, Jérémie Giraud, Vitaliy Ogarko, Sébastien Chevrot, Stephen Beller, Pascal Gegout, Mark Jessell

### ► To cite this version:

Roland Martin, Jérémie Giraud, Vitaliy Ogarko, Sébastien Chevrot, Stephen Beller, et al.. Three-dimensional gravity anomaly inversion in the Pyrenees using compressional seismic velocity model as structural similarity constraints. *Geophysical Journal International*, 2020, 10.1093/gji/ggaa414 . hal-02989587

**HAL Id: hal-02989587**

**<https://hal.science/hal-02989587>**

Submitted on 23 Nov 2020

**HAL** is a multi-disciplinary open access archive for the deposit and dissemination of scientific research documents, whether they are published or not. The documents may come from teaching and research institutions in France or abroad, or from public or private research centers.

L'archive ouverte pluridisciplinaire **HAL**, est destinée au dépôt et à la diffusion de documents scientifiques de niveau recherche, publiés ou non, émanant des établissements d'enseignement et de recherche français ou étrangers, des laboratoires publics ou privés.

# 1 **Three-dimensional gravity anomaly inversion in the** 2 **Pyrenees using compressional seismic velocity model as** 3 **structural similarity constraints**

4 Roland Martin<sup>1</sup>, Jérémie Giraud<sup>2</sup>, Vitaliy Ogarko<sup>2,3,4</sup>, Sébastien Chevrot<sup>1</sup>,  
*Stephen Beller<sup>1</sup>, Pascal Gégout<sup>1</sup> and Mark Jessell<sup>2</sup>*

<sup>1</sup> *Laboratoire de Géosciences Environnement Toulouse GET, CNRS UMR 5563, Observatoire Midi-Pyrénées,  
Université Paul Sabatier, 14 avenue Édouard Belin, 31400 Toulouse, France*

<sup>2</sup> *Centre for Exploration Targeting, School of Earth Sciences,  
University of Western Australia, 35 Stirling Highway, 6009, Crawley, Australia*

<sup>3</sup> *International Centre for Radio Astronomy Research (ICRAR), University of Western Australia, 7 Fairway, Crawley WA 6009*

<sup>4</sup> *ARC Centre of Excellence for all Sky Astrophysics in 3 Dimensions (ASTRO 3D)*

## 5 6 **SUMMARY**

7  
8 We explore here the benefits of using constraints from seismic tomography in gravity  
9 data inversion and how inverted density distributions can be improved by doing so. The  
10 methodology is applied to a real field case in which we reconstruct the density struc-  
11 ture of the Pyrenees along a southwest-northeast transect going from the Ebro basin in  
12 Spain to the Arzacq basin in France. We recover the distribution of densities by invert-  
13 ing gravity anomalies under constraints coming from seismic tomography. We initiate the  
14 inversion from a prior density model obtained by scaling a pre-existing compressional  
15 seismic velocity  $V_p$  model using a Nafe-Drake relationship : the  $V_p$  model resulting from  
16 a full-waveform inversion of teleseismic data. Gravity data inversions enforce structural

17 similarities between  $V_p$  and density by minimizing the norm of the cross-gradient be-  
18 tween the density and  $V_p$  models. We also compare models obtained from 2.5D and 3D  
19 inversions. Our results demonstrate that structural constraints allow us to better recover  
20 the density contrasts close to the surface and at depth, without degrading the gravity data  
21 misfit. The final density model provides valuable information on the geological struc-  
22 tures and on the thermal state and composition of the western region of the Pyrenean  
23 lithosphere.

24 **Key words:** Gravity Modelling – Data inversion – Seismic correlation and constraints –  
25 Computational geophysics – Numerical modelling

## 26 1 INTRODUCTION

27 During the last decade, seismic full waveform inversion has become a powerful and an increasingly  
28 popular technique for Earth imaging (Tarantola & Valette 1982a,b; Virieux & Operto 2009; Monteiller  
29 et al. 2013, 2015). However, with this method, density is retrieved with a lower resolution compared to  
30 seismic velocities or Lamé parameters, and is often not sufficiently reliable for interpretation. Recov-  
31 ery of density from seismic data alone is difficult and may require the utilisation of prior information  
32 (Alemie & Sacchi 2011; Lines 1999). Gravity data inversion is the common way of retrieving densities  
33 but has a poor depth resolution and thus needs additional constraints. In this context, complementarity  
34 with seismic data has been recognized (Lelievre et al. 2012) as seismic tomography provides seis-  
35 mic velocity models that can be exploited jointly with gravity data for improved subsurface density  
36 imaging. Another motivation to perform gravity inversion constrained by seismic modeling is that  
37 densities inferred from compressional seismic velocity models through Nafe-Drake or linear scaling  
38 relationships may be affected by significant uncertainties that can exceed 10% (Herceg et al. 2015).  
39 One of our main motivations is thus to reduce significantly these uncertainties by recovering densities  
40 through gravity field data inversion constrained by seismic velocities, thereby preserving physical and  
41 structural similarities between seismic velocities and densities.

42 Another long-term goal is to refine existing density models at depth to get insights into the composition  
43 and thermal state of the lithosphere and to confront inverted models with existing geological models.  
44 In this perspective, we use teleseismic FWI (TFWI) tomography as a priori information to constrain  
45 gravity inversion and to refine existing density models. Scaling laws provide useful information on  
46 density from crustal compressional velocity ( $V_p$ ) models (Brocher 2005) that can be used as prior in-  
47 formation to constrain solutions of gravity inversion at lithospheric scale. In this context, we exploit

48 the results of TFWI on data collected in the Western Pyrenees during the 2009-2014 PYROPE and IB-  
49 ERARRAY seismic experiments (Chevrot et al. 2014, 2015, 2018) to constrain the inversion of gravity  
50 data provided by the BGI/Bureau Gravimétrique International (International Gravimetry Bureau). A  
51  $V_p$  seismic model has been obtained by full waveform of teleseismic P-waves recorded in the western-  
52 most PYROPE transect (Wang et al. 2016) in a 3D slice crossing the gravity anomaly of Mauleon's  
53 basin. This 3D slice was involving the seismic profile surrounded by temporary seismic stations to  
54 constrain laterally the TFWI. In a previous study in this region, where the strongest gravity anomalies  
55 in France are present (Martin et al. 2017), we reconstructed density distributions with an unconstrained  
56 gravity inversion procedure but densities still remained poorly constrained at depth. A conclusion of  
57 that study was that further inversions were needed with additional constraints and prior information to  
58 provide robust images of deeper structures : without sufficient prior information, gravity inversion is  
59 heavily affected by non-uniqueness and the inverse problem suffers from rank deficiency. Here, we in-  
60 troduce supplementary structural similarity constraints in the gravity data cost function minimization.  
61 We formulate these similarity constraints via cross gradients (e.g., Gallardo & Meju (2003)) between  
62 density and  $V_p$  models to obtain 3D density models that are consistent simultaneously with TFWI  
63 results and gravity data. In a similar work but more focused on offshore basin modelling, Welford  
64 et al. (2018) performed 3D gravity modeling to obtain 3D density models constrained by structural  
65 models derived from seismic tomography. More recently, Darijani et al. (2020) obtained 2D density  
66 models through a 2D gravity inversion constrained by a 2D seismic model at the near surface scale via  
67 a clustering/ petrophysical constraint approach as in Lelievre et al. (2012). In our study, we rely on a  
68 3D model coming from TFWI and therefore we do not need such petrophysical/clustering constraints.  
69 We introduce implicitly those constraints via a Nafe-Drake scaling relationship between density and  
70  $V_p$ .

71 Similar ideas have been proposed in other related works by Saunders et al. (2005) in the con-  
72 text of resistivity inversion constrained by seismic data, and by Brown & Singh (2012) and Yan &  
73 Garcia Juanatey (2017) for electromagnetic and magnetotelluric data inversion constrained by fixed  
74 seismic structures. Using linear relations between seismic velocities and densities or cross-gradient  
75 constraints between seismic velocities, densities and magnetic susceptibilities, Colombo & Stefano  
76 (2007), Stefano et al. (2011), and Moorkamp et al. (2011) performed joint inversion of seismic, gravity  
77 and electromagnetic data. In these earlier studies, seismic tomography relied essentially on ray-theory  
78 methods. Blom et al. (2017) performed a joint full waveform/gravity data inversion for a global scale  
79 application, and found that additional seismic velocity-density correlations or structural constraints are  
80 needed to properly reconstruct density anomalies. Lin & Zhdanov (2019) used the joint seismic and  
81 gravity data inversion to image a synthetic salt-dome model. The method is constrained by a Gramian

82 stabilizer applied to the gradient of seismic velocities and densities to increase the correlation be-  
83 tween the different physical parameters of the inverse model or their spatial gradients. In Giraud et al.  
84 (2019b), gravity data inversions were constrained by geological structural uncertainty using entropy  
85 arguments.

86 This article is organized as follows. After introducing the geophysical and geological context of  
87 this study, we describe in a second part our inversion methodology and the optimization process. We  
88 then explain how to appropriately weight the different constraint terms involved in the cost function to  
89 be minimized and we show the models obtained after inversion. Then we present solutions of two kinds  
90 of gravity data inversions constrained by the  $V_p$  model: a 2.5D gravity data inversion of a 1D Bouguer  
91 anomaly profile aligned with the seismic transect and a 3D inversion of the available gravity data in  
92 the 3D slice area. For the 2.5D gravity inversion, the 2.5D prior model is built by taking a 2D vertical  
93 section extracted from the 3D TFWI model and extended along either the direction perpendicular to  
94 the seismic profile or along the strike of the Pyrenees. As expected, we show that both the width and  
95 the strike of the anomalies influence the gravity response. However, the finite extent of the anomalies  
96 has a more dominant contribution than the orientation of the strike. All our 2.5D tests show that the  
97 lateral extension of the Mauleon's anomaly must be finite, with a width of about 30 km. We performed  
98 a 3D inversion to laterally localize the density anomalies, the 2.5D not being able to do it. The 2.5D  
99 inversions helped us to estimate the order of magnitude of the hyperparameters of regularization and  
100 to refine more quickly the range of the hyperparameters for the 3D inversions. Finally, we compare  
101 the different inverted models that we obtained in the 2.5D and 3D cases and propose a preliminary  
102 geological interpretation of our findings.

## 103 **2 GEOLOGICAL AND GEOPHYSICAL CONTEXT**

### 104 **2.1 Geology of the area**

105 The Pyrenees result from the collision between Iberia and Eurasia from late Cretaceous to early  
106 Miocene (Lescoutre 2019; Lescoutre & Manatschal 2020; Gómez-Romeu et al. 2019). Positive com-  
107 plete Bouguer gravity anomalies characterize the northern flank of the Pyrenees, which are particularly  
108 strong in the Mauleon basin and close to the town of Saint-Gaudens (section A-A' in Figure 1-a). Un-  
109 derstanding the nature and origin of these anomalies (from the upper mantle or from shallow crust  
110 structures) has been a long-lasting controversy, and was one of the main motivations of the PYROPE  
111 and IBERRARRAY seismic deployments from 2009 to 2014 (Chevrot et al. 2014, 2015), and of the  
112 later OROGEN deployments from 2015 to 2017 (Chevrot et al. 2018). Another motivation for study-  
113 ing the western part of the Pyrenees is that this region is seismically more active than the eastern part

114 (Souriau & Pauchet 1998). In particular it presents a pronounced concentration of seismicity beneath  
 115 the northern Pyrenean foothills that is not observed in the eastern Pyrenees. This feature may be related  
 116 to the strong structural asymmetry of the Pyrenees, with a continental subduction in the central and  
 117 western Pyrenees that is absent in the eastern Pyrenees (Chevrot et al. 2018). Recently, FWI has been  
 118 applied to teleseismic  $P$  waves recorded along the westernmost PYROPE profile, complemented with  
 119 data recorded by nearby permanent stations. The resulting 3D  $V_p$  model (Figure 2), which resolved the  
 120 structures over a band of 60 km surrounding the profile, revealed the presence of a shallow mantle  
 121 body at 10 km depth below the Mauleon basin (Wang et al. 2016; Martin et al. 2017; Chevrot et al.  
 122 2018). This mantle body, probably exhumed during the Cretaceous episode of rifting, explains the  
 123 large positive Bouguer anomalies shown in Figure 1-b.

124 As mentioned in Martin et al. (2017), FWI can provide compressional and shear velocities as well  
 125 as densities but in practice density is not really well reconstructed by FWI alone (Wang et al. 2016;  
 126 Beller et al. 2017). Therefore, adding gravity data into the inversion can improve the density model  
 127 reconstruction. Here, we aim at inverting a complete Bouguer gravity anomaly data set extracted from  
 128 the BGI database under the constraint of a  $V_p$  model obtained by inverting teleseismic  $P$  waveforms  
 129 recorded by the westernmost PYROPE profile (Chevrot et al. 2015).

## 130 2.2 Geophysical data and prior information for inversion

131 To perform gravity inversion constrained by compressional velocity models, we consider the dense  
 132 (65062 points) complete Bouguer gravity anomaly dataset from the BGI database covering the French  
 133 and Spanish continental regions (see the map of measured Bouguer gravity data in Figure 1a). These  
 134 data have been used to obtain a 2 mn arc gridded global model of the complete Bouguer gravity  
 135 anomalies (Balmino et al. 2012; Geodesist's-Handbook 2012) shown in Figure A1. For our study we  
 136 preferred to use directly the measured data instead of the gridded data in order to make computations  
 137 at the measurement points for maximum accuracy in the calculations. From this measured dataset, we  
 138 extract a subset of 13000 points that are projected on a regular 2700 ( $135 \times 20$ ) points grid (340 km  
 139 long  $\times$  50 km wide and rotated  $45^\circ$  eastward) that includes the westernmost (A-A') 2.525 km reso-  
 140 lution transect imaged by TFWI (See Figures 1b and 1c). This seismic profile runs from coordinates  
 141 ( $-2.615^\circ$ ,  $42.071^\circ$ ) to ( $0.32167^\circ$ ,  $44.4323^\circ$ ) and crosses the Ebro and Mauleon basins. Those 2700  
 142 gravity data points, located up to 25 km from the transect are used for 3D inversion and are also inter-  
 143 polated along this profile (136 points with a 2.525 km spacing) for 2.5D inversion. Along the profile,  
 144 gravity anomalies show strong variations across the Pyrenees with anomalies, varying between -90  
 145 mgal in the south to +30 mgal in the north.

146 We now define the 3D a priori density model of the western Pyrenees that will be used in our

147 Bouguer anomaly inversions. The density model is first constructed by extracting a  $V_p$  volume around  
 148 the seismic profile mentioned before. We scaled the a priori density model  $\rho$  using this  $V_p$  model and  
 149 using the Nafe-Drake law (Nafe & Drake 1957; Ludwig et al. 1970; Brocher 2005) as in Martin et al.  
 150 (2017):

$$\rho = 1.6612V_p - 0.4721V_p^2 + 0.0671V_p^3 - 0.0043V_p^4 + 0.000106V_p^5, \text{ for } V_p < 7.4 \text{ km/s} \quad (1)$$

and

$$\rho = \rho_m = 3270 \text{ kg/m}^3, \text{ for } V_p > 7.4 \text{ km/s} \quad (2)$$

151 We define the density anomalies  $\Delta\rho = \rho - \rho_c$  in the crust (from the upper surface down to a  
 152 reference Moho depth of 30 km) as the deviation from a reference crustal density  $\rho_c = 2670 \text{ kg/m}^3$ ,  
 153 and  $\Delta\rho = \rho - \rho_m \text{ kg/m}^3$  beneath the Moho for a reference upper mantle density  $\rho_m$  (at depths larger  
 154 than 30 km). The 3D prior density model is shown Figure 3 with different cut sections at different  
 155 depths (16.4 km, 50 km). Predicted Bouguer gravity anomalies (Figure 1-b) are relatively close to the  
 156 measured Bouguer anomaly in the central and northern part of the profile. In our numerical tests, we  
 157 have also observed that computed gravity responses are not influenced by density structures located  
 158 farther than 25 km from the transect. As in Martin et al. (2017), a 340 km long  $\times$  50 km wide  $\times$  75  
 159 km deep 3D inner computational domain is considered and discretized over  $136 \times 20 \times 30$  prismatic  
 160 bodies ( $2.525 \text{ km} \times 2.525 \text{ km} \times 2.533 \text{ km}$  volume per cell). An external tapering is added to the inner  
 161 computational domain (see Figure 5) in order to avoid edge effects. It involves 20 extra cells on each  
 162 vertical outer interface of the computational domain. The 1 mn arc ( $\approx 1.78 \text{ km}$ ) ETOPO1 topography  
 163 is added and interpolated at a resolution of 2.525 km resolution in longitude and latitude on top of the  
 164 computational mesh. The gravity measurements are projected on this topography grid (Figures 4 and  
 165 5). Furthermore, the computational mesh is distorted close to the surface to follow the topography.

166 The 2.5D models are built by extracting 2D  $V_p$  and density sections from the 3D TFWI models  
 167 along the transect and by replicating them invariantly to themselves over a 30 km (Figure 6-A) or a  
 168 44 km width (Figure 6-B). They are rotated with different angles  $\theta$  with respect to the A-A' profile  
 169 from 0 degree, which corresponds to the direction perpendicular to A-A' (line P-P') to 45 degrees  
 170 which corresponds approximately to the strike of the Pyrenees (S-S' in Figure 4). In Figure 6, we  
 171 show the influence of the angle of rotation and width of different 2.5D a priori models on the gravity  
 172 response. For a 44 km width, the gravity anomalies are overestimated by a large amount for all angles  
 173 of rotation (Figure 6-B), while for a 30 km width the gravity anomalies are in good agreement with the  
 174 observed data. For a 30 km width and angles of 0 to 25 degrees, the amplitudes are very similar and are  
 175 overestimated by 2-4 mgals while for 45 degrees they are underestimated by 2 mgals approximately.

176 This suggests that the strong anomaly produced by the shallow mantle body beneath the maximum  
 177 gravity anomaly is oriented along a direction close to the strike of the Pyrenees (at an angle between  
 178 30 and 40 degrees from the P-P' transect). This width and those angles are close to those estimated  
 179 ( $\simeq 24$  km width) at the the first order by Wang et al. (2016). However, note that for narrow density  
 180 anomalies their orientation has a secondary effect compared to their lateral extent.

### 181 3 STRUCTURALLY CONSTRAINED INVERSION METHOD

182 Starting from a Nafe-Drake scaled density model as defined in the previous section, we explain now  
 183 to perform the gravity data inversion under structural similarity constraint of densities by minimizing  
 184 the cross-gradient between density and a fixed seismic velocity model obtained from TFWI.

#### 185 3.1 Structural constraints

186 In our constrained inversion, structural correlations are taken into account between density anomalies  
 187  $\Delta\rho$  and compressional velocities  $V_p$ . We assume that at any point in the medium there exists, to first  
 188 order, a spatially varying parameter  $\beta$  such that  $\nabla\Delta\rho = \beta\nabla V_p$ . Here, we consider the  $V_p$  model  
 189 obtained through TFWI as a suitable structural model describing the deep crustal architecture.

190 The structural constraints we apply here consist of minimizing the cross-gradient between density  
 191 and velocity anomalies similarly to the joint resistivity-velocity inversion procedure used by Gallardo  
 192 & Meju (2003) and by many others since then (Meju & Gallardo 2016). Imposing a zero cross-gradient  
 193 between two model distributions is equivalent to imposing local colinearity between the spatial gradi-  
 194 ents of the two models. The advantage of using the cross-gradient in our study is that we do not need  
 195 to impose any predefined linear correlation function or any coefficient  $\beta$  in the inversion.

#### 196 3.2 Inverse problem formulation and resolution

Let us now describe our methodology for gravity data inversion under seismic constraints. We min-  
 imize a cost function  $\chi$  that involves the misfit between measured and computed complete Bouguer  
 gravity anomalies, and regularize the problem by adding a damping of the norm of the density anomaly  
 model  $\Delta\rho$  and a structural constraint using the cross-gradient between density and  $V_p$  models. The to-  
 tal cost function is thus

$$\chi(m) = \| D_{obs} - D_{cal} \|^2_{l^2} + \lambda^2 \| W(\Delta\rho - \Delta\rho_p) \|^2_{L^2} + \alpha^2 \| \nabla\Delta\rho \wedge \nabla V_p \|^2_{L^2}, \quad (3)$$

where  $\Delta\rho$  is the density anomaly,  $\Delta\rho_p$  the prior density anomaly,  $D_{obs}$  and  $D_{cal}$  the measured and the-  
 oretical Bouguer gravity data, and  $\lambda$  and  $\alpha$  the regularization weights applied to the density model and

the cross-gradients respectively.  $W$  is a depth weighting operator applied on the model and computed by integrating the sensitivity gravity kernel  $S$  over the whole mesh volume and for each observation point location (Portniaguine & Zhdanov 2002). For the density anomaly in cell  $k$  of the computational mesh, this matrix operator  $W$  is defined as

$$W_{kk} = \sqrt{\left(\sum_{i=1, N_{obs}} S_{i,k}^2\right)^{1/2}}, \quad (4)$$

197 where  $S_{ik}$  is the element of the gravity kernel  $S$  linking the density anomaly  $\Delta\rho_k$  in cell  $k$  to the  
198 gravity anomaly  $D_{cal}^i$  at location  $x_i$  such that  $D_{cal}^i = S_{ik}\Delta\rho_k$ .

199 The cross-gradient is discretized in space using a finite-difference scheme. In our Tomofast-x  
200 parallel inversion platform, we minimize Equation (3) using the LSQR algorithm of Paige & Saunders  
201 (1982), which is implemented using a parallelized sparse matrix solver. At each inversion cycle (i.e.,  
202 outer loop of LSQR inversion), the model is updated using an approximate solution using a fixed  
203 number of iterations in the inner loop of the LSQR algorithm (Martin et al. 2013, 2018; Giraud et al.  
204 2019a,b).

## 205 **4 NUMERICAL RESULTS OF THE STRUCTURALLY CONSTRAINED INVERSION**

### 206 **4.1 Weighting of cost function terms in the 2.5D and full 3D inversion cases**

207 To minimize the aggregate cost function (3) it is crucial to achieve optimum balancing between the  
208 different contributing terms. We determine the optimum weights  $\lambda$  and  $\alpha$  following a L-curve approach  
209 (Hansen and O’Leary, 1993), which we extend to the two-parameter case by using a strategy similar  
210 in spirit to the Pareto optimization scheme (Bijani et al. 2017).

211 Our analysis is based on the minimization of the data misfit cost function (term 1 in equation  
212 (3), Figure 7-a), the model norm (term 2 in equation (3), Figure 7-d), cross-gradient norm (term 3 in  
213 equation (3), Figure 7-c) and the aggregate global cost function  $\chi$  in equation (3), black solid curve in  
214 Figure 7-e). In Figure 7-b, we show the behavior of the cross-gradient and the model norms for a low  
215 data misfit of  $10^{-4}$ . We estimate the optimum  $(\lambda, \alpha)$  values by identifying the inversion case fulfilling  
216 a series of conditions in terms of data misfit (Figure 7-a), model norm (Figure 7-d), and cross-gradient  
217 (Figure 7-c) values. The method has been applied to the four 2.5D a priori models rotated by 0, 20, 25  
218 and 45 degrees respect to the P-P’ direction. Similar inverted solutions have been obtained in the four  
219 cases and similar  $(\lambda, \alpha)$  regularization parameters have been obtained. We describe now how those  
220 hyperparameters have been obtained for the 2.5D case (for 0 degrees for instance) and also for the 3D  
221 inversion and we present and compare the 2.5D and 3D results.

222 The process to determine  $\lambda$  and  $\alpha$  is divided in three main stages. We first analyse a population

223 of inverted models obtained from inversions using a range of values sampled on a discretized  $(\lambda, \alpha)$   
 224 grid. To accelerate the search, we take a 2.5D a priori model averaged along the (A-A') transect that  
 225 is extended invariantly to itself over 12 cells perpendicularly to the right and left of the profile. In our  
 226 study, the  $(\lambda, \alpha)$  grid consists of 11 x 11 values and is used to generate a collection of 121 inverted  
 227 models. In a second stage, from this set of models, we then define a refined subrange of values thought  
 228 to contain the optimum  $(\lambda, \alpha)$  pair. In this refined subrange, here taken as  $[10^{-8}, 5 \cdot 10^{-5}] \times [10^{-5},$   
 229  $10^{-1}]$ , we refine the weights sampling around the optimal values. To this end, we perform 21 x 19  
 230 inversions on a refined set of  $(\lambda, \alpha)$  pairs.

231 The estimate of the optimum set of weights (see Figure 7-a) that balance the contribution of  
 232 the different terms is obtained by identifying the case with lowest overall cost among the subset of  
 233 inverted models honoring all the conditions (see Figure 7-e). In these 2.5D inversions, we choose a  
 234 damping model parameter  $\lambda = 3.5 \times 10^{-7}$  and a cross gradient weight  $\alpha = 2.3 \times 10^{-4}$ . To ensure  
 235 appropriate balancing between the different terms of the cost function, the optimum weights of the  
 236 different terms have been inferred from the inflection points in the curves of data misfit curve versus  
 237 model perturbations and cross-gradient norm (Figures 7-b,c,d). We apply the L-curve analysis by  
 238 performing many inversion runs with different  $\lambda$  and  $\alpha$  values. An example is taken along the dashed  
 239 lines shown in Figure 7-e where the optimum  $\alpha$  value is determined and fixed and an optimum  $\lambda$  value  
 240 is determined accordingly. In a third stage, once the optimal values of the damping model parameter  
 241  $\lambda$  and of the cross gradient weight  $\alpha$  have been found in 2.5D, we perform the inversions over the  
 242 full 3D heterogeneous model with values of  $\lambda$  and  $\alpha$  finely tuned around the values obtained in the  
 243 previous 2.5D case.

## 244 **4.2 Cross-gradient constraints and their influence on density model reconstruction : the 2.5D** 245 **case example**

246 To show the impact of an a priori model and the different penalty terms of the misfit function on the  
 247 inverted solutions, we performed different tests with or without damping or cross-gradient penalty  
 248 in the misfit function. For the sake of clarity, the results of constrained and unconstrained inversions  
 249 are described in appendix B for the 2.5D model example (i.e for an a priori 3D model defined as a  
 250 Nafe-Drake scaled density model extrapolated in the direction P-P' orthogonal to the A-A' profile).  
 251 As shown in Figure A2, the data misfit function is well minimized in all cases, which suggests that  
 252 the solution of the inverse problem is not unique. To obtain physical solutions at depth, as discussed  
 253 in appendix B and observed in figure A3, it is thus crucial to perform the inversions considering  
 254 all the terms of the total cost misfit function. We now focus our attention on the inverted solutions  
 255 obtained under constraints. In Figure 9 we show the differences between inverted solutions obtained

256 for the prior density model extracted from the TFWI model and extrapolated invariantly to itself in  
257 directions making an angle  $\theta$  with the transect P-P' perpendicular to the A-A' profile. For  $\theta=0$ , the  
258 model is invariant in the direction P-P' and for  $\theta = 45$  degrees it is invariant along the S-S' direction  
259 parallel to the strike of the Pyrenees passing through the highest Mauleon's gravity anomaly. As we  
260 can see, the differences are rather small, with maximum absolute differences and standard deviations  
261 of approximately 4 and  $1.5 \text{ kg m}^3$  obtained for the 45 degrees case. The solutions are very close with  
262 a small but noticeable difference close to the surface. Again, these small differences result from the  
263 limited lateral extent of the anomalies as it was already the case for the responses of the four a priori  
264 models used in those 2.5D inversions.

265 For the 2.5D density modeling case, we first minimize the misfit cost function without the cross-  
266 gradient term and we obtain a density distribution that is not well constrained at depth (Figure 8) as  
267 in Martin et al. (2017). As already mentioned, instead of normalizing the sensitivity matrix by a depth  
268 weighting function, we use the integrated sensitivity technique of Portniaguine & Zhdanov (2002). The  
269 differences between inverted and prior density models are shown in Figure 8. The solution is obviously  
270 not geologically relevant because the model perturbations are mainly concentrated close to the surface  
271 and decrease continuously with depth. To alleviate this, we take the same prior model and we now  
272 minimize the cost function with the cross-gradient constraint. This time, we obtain well constrained  
273 densities at depth with density perturbations that follow the spatial variations of the  $V_p$  model (see the  
274 evolution of the cross-gradient in Figure 10). After 200 successive inversion cycles, the cross gradients  
275 are minimized in the first 60 km depth. In the first inversion cycles, the cross gradients are strong, but  
276 they progressively decrease and tend to very low values not only close to the surface but also at depth.  
277 Note that the differences between a priori and inverted densities are as pronounced at depth as they  
278 are closer to surface (Figure 8-bottom). We note that this feature is not possible to achieve without  
279 geometrical/structural constraints. In Figure 7-e we can see the evolution of the different terms of the  
280 whole cost function that reaches a value of  $10^{-7}$  after 20 successive LSQR inversions (outer loop) with  
281 300 iterations for each LSQR inversion. At the end of the inversion the cost function reaches a value  
282 of approximately  $4 \times 10^{-8}$  and the data misfit has decreased by more than 80% (see Figure 7-e). The  
283 2.5D inversion helps to tune the penalty parameters. However, it does not take into account correctly  
284 nor the localization of the lateral heterogeneities neither their orientation in the vicinity of the A-A'  
285 profile. It tends to concentrate the density perturbations along the central profile due to a different  
286 geometrical divergence of the gravity fields and also to decrease the density anomaly values below the  
287 location of strong gravity anomalies. It is thus always preferable to perform a full 3D inversion that  
288 allows to localize the density anomalies below strong gravity anomalies are present and also to better  
289 define their orientation.

### 290 4.3 Full 3D inversion case using topography

291 In order to have better images in the direction perpendicular to the profile, we perform gravity in-  
 292 versions for  $\alpha$  and  $\lambda$  values ( $\lambda = 2 \times 10^{-7}$  and  $\alpha = 10^{-3}$ ) close to the optimal values obtained  
 293 previously in the 2.5D case. As starting and a priori model we take the density model scaled with the  
 294 3D  $V_p$  model obtained by FWI according to the Nafe-Drake law. The inner computational domain is  
 295 the same as previously. However, a padding of 20 cells has been added to each outer vertical edge of  
 296 the model to avoid edge effects. The 3D model has thus a total size of  $175 \times 60 \times 30$  grid points.  
 297 We perform 100 LSQR inversion cycles (outer loop) to achieve enough convergence of the whole in-  
 298 version algorithm until reaching a total cost function value of  $3.6 \times 10^{-7}$ . Gravity data are very well  
 299 reproduced with point-to-point absolute errors lower than 0.4 mGal ( $4 \times 10^{-6} \text{ m/s}^2$ ), a total data misfit  
 300 contribution of  $5.46 \times 10^{-8}$  to the total misfit function, and a global relative error of  $2.235 \times 10^{-3}$ .  
 301 Figure 12 shows the final model along the A-A' profile in a vertical section and also in a horizontal  
 302 plane located at a 16.4 km depth (Figure 12-a), as well as in a section P-P' perpendicular to the profile  
 303 (in the direction of the axis of the Pyrenees, Figure 12-d). Inverted densities are showing variations of  
 304 +/- 130 kg/m<sup>3</sup> slightly higher than to those obtained for the 2.5D inversion (+/- 100 kg/m<sup>3</sup>). Density  
 305 anomalies close to the Moho are showing clear subduction of the Iberian plate beneath the European  
 306 plate (negative density anomaly below 30 km depth) with part of the European Mantle rising up close  
 307 to the surface (strong positive anomaly above the 30 km reference Moho depth). Indeed, in Figure 12,  
 308 the new model emphasizes the subduction of the Iberian plate (represented by a strong negative den-  
 309 sity anomaly in blue) and the presence of exhumed mantle material (evidenced by a positive anomaly,  
 310 high red values) reaching a  $\simeq 10$  km depth. In the section perpendicular to the Pyrenean axis (Figure  
 311 12-d), the 3D inversion constrains the width of the exhumed mantle body to about 20 km in agree-  
 312 ment with the 2.5D inversions (Wang et al. 2016). However, the 3D full modeling provides a better  
 313 reconstruction of the geometry of the anomalies in particular of the shallow mantle body, with better  
 314 localization, orientation, and more accurate width. Furthermore, the exhumed anomaly can be located  
 315 laterally, which is not possible by construction in the 2.5D configuration. This can be observed in  
 316 Figure 12-a on the section located at a depth of 16.4 km, where the exhumed mantle anomaly is not  
 317 exactly on the A-A' axis but is rotated with an angle of about 45 degrees with respect to P-P' direction.  
 318 The remaining differences between inverted and a priori models are mainly observed in the Iberian-  
 319 European collisional domain. The initial cross-gradients are lower than those of the 2.5D case by an  
 320 order of magnitude everywhere. Below 20 km depth, they are decreasing from about  $4 \times 10^{-3}$  down  
 321 to  $1.5 \times 10^{-3}$  after inversion. At 5-10 km depth, cross-gradients are also reduced but remain important  
 322 on top of the exhumed mantle body. In general, gravity data alone allow us to recover densities close

323 to the surface but not at depth. But, thanks to the cross-gradient, we can also constrain deep density  
324 anomalies.

325 In Figure 13, a dispersion diagram between density and  $V_p$  is shown for constrained and uncon-  
326 strained solutions, and compared with the Nafe-Drake reference scaling. As in Martin et al. (2017),  
327 the densities obtained without  $V_p$  similarity constraints are overestimated and density values lower  
328 than  $2550 \text{ kg/m}^3$  are almost absent close to the surface level and at depth. Moreover, adding the cross-  
329 gradient constraint increases the amplitude of the variations of the densities compared to the densities  
330 obtained without cross-gradient constraints: it decreases further the densities where anomalies are neg-  
331 ative close to the surface and also at depth until reaching the crust-mantle transition. This reduction  
332 has an amplitude ranging between  $-130$  and  $+130 \text{ kg/m}^3$ . We now obtain lower densities in the crust  
333 and close to the surface in agreement with the results of Grandjean (1994) in which densities are lower  
334 than  $2500 \text{ kg/m}^3$  in the first 7 km in the basins.

## 335 5 GEOLOGICAL AND GEOMECHANICAL INTERPRETATION

336 Visually, the recovered density model bears important similarities with the tomographic model of  
337 Wang et al. (2016), as can be seen in Figure 14. The model is also coherent with the recent collision  
338 models of Lescoutre (2019) (chapter III, Figure p.121, and Figure III-4, p. 131) and Lescoutre &  
339 Manatschal (2020); Gómez-Romeu et al. (2019). Our inversions show that the European mantle wedge  
340 and the Gavarnie nappe have strong imprint in the density model, with strong negative and positive  
341 density contrasts respectively (see Figure 12-c-left). The exhumed mantle body and the Gavarnie thrust  
342 show geometries in good agreement to the northern part of their transect passing through the Eastern  
343 part of Mauleon basin (profile A in Lescoutre (2019), Chapter III, Figure p.121). The southernmost  
344 part of our model is more similar to the geological profile passing through the west of Mauleon basin  
345 (profile B in Chapter III, p.121 Lescoutre (2019), reproduced in appendix A.5). Again, this simply  
346 results from the strong obliquity of the seismic transect with respect to the strike of the Pyrenees. Our  
347 3D imaged section corresponds also to the profile passing through the Ebro basin and eastern Mauleon  
348 (section in of Figure III-4 of Lescoutre (2019), p. 131) and reproduced also in Figure A.5. In short,  
349 the AA' model profile (Figure 1) can be seen as an intermediate stage between these two south-north  
350 transects : one passing through the Eastern Mauleon basin and another one passing through Saint-Jean  
351 de Luz basin and Ebro basin at the west of Mauleon basin, with a central part where the geometry of  
352 the mantle body is in good agreement with Wang et al. (2016).

353 We computed the Airy isostatic gravity anomalies by taking a reference Moho model obtained by  
354 assuming a 30 km compensation depth and topography interpolated from a ETOPO1 (1mn resolution).  
355 Reference isostatic densities of  $2670 \text{ kg/m}^3$  above this Moho and  $3270 \text{ kg/m}^3$  beneath are used. In

356 Figure 15, the observed isostatic anomalies are very similar to the isostatic anomalies computed in the  
357 final density model (i.e after inversion). The isostatic anomalies are reduced in the southern part of the  
358 profile compared to the Bouguer anomalies due to surface topography which predicts a deeper Moho  
359 (reaching around 36 km depth) that partly compensates the topography in that region, which is not the  
360 case in the northern part. The differences between observed and calculated anomalies are very small  
361 and reach maximum errors lower than 1 mGal (as can also be seen in Figure 12-d). This comparison  
362 demonstrates that it is equivalent to invert either Bouguer or isostatic anomalies.

## 363 6 CONCLUSIONS

364 We have performed 2.5D and full 3D gravity data inversions in the region showing the strongest gravity  
365 anomalies in the Pyrenees using structural constraints derived from a tomographic  $V_p$  model to favor  
366 structural similarities between seismic velocity and density models. These constraints improved the  
367 density models at depth, by transferring structural information from TFWI to the density model, and  
368 providing structural details of the mantle wedge and the upper crust structures. Full 3D inversions with  
369 topography allow us to take into account lateral variations of densities and to localize heterogeneities  
370 at depth more accurately than with 2.5D inversions. 3D inversions also tend to better define their  
371 orientation (along the strike of the Pyrenees), whereas 2.5D inversions tend to decrease anomalies and  
372 concentrate them closer to the surface and along the central plane. The structural constraints adjust  
373 the densities not only close to the surface but also at depth close to the Moho with up to 10% density  
374 variations. However, 2.5D inversions allow us to tune quickly a range of penalty parameters of the  
375 cost function that can be used to estimate penalty hyperparameters for the full 3D inversions. These  
376 3D inversions can be run in less than 20 minutes on 256 Intel Skylake 2.3GHz cores of the Olympe  
377 supercomputer. Inverting Bouguer or isostatic anomalies can be equivalently done and gives similar  
378 density models. They only differ by a shift generated by the removal of the reference Moho depth  
379 perturbation from the Bouguer anomalies.

380 In a future and second step, our methodology will be applied in 3D to the rest of the Pyrenees.  
381 Future work will include joint cross-gradient inversion of gravity and seismic data at the scale of  
382 the whole Pyrenees. We will also consider adding constraints such as petrophysical and geological  
383 information as in Wehr et al. (2018). In the present study, we performed inversions on medium sized  
384 supercomputing resources (50 to 200 processors clusters) but for the inversion of the whole Pyrenees  
385 area much more processors will be needed (at least 10 to 20 times more). In the mid-term, having  
386 access to the densities will provide key information on the mineralogic composition and thermal state  
387 of the lithosphere. To this end a full joint inversion seems to be a promising way to improve our  
388 capacity to image internal Earth structures by reducing model uncertainties.

**ACKNOWLEDGMENTS**

We thank the CALMIP supercomputing mesocentre of Toulouse, France, for their support through project P1138 on the Olympe supercomputer platform, and the TGCC/GENCI supercomputing center through project gen6351 on the CURIE supercomputer. We are grateful to the CNES granted projects 2017 and 2018-TOSCA/GET-GRAVI-GOCE for their financial support. This study was also supported by the Orogen research project, a tripartite academic-industry collaboration between CNRS, BRGM and Total. Jeremie Giraud was also supported by an Australian Government Research Training Program (RTP) Scholarship when part of this work was conducted.

## 397 REFERENCES

- 398 Alemie, W. & Sacchi, M. D., 2011. High-resolution three-term avo inversion by means of a trivariate cauchy  
399 probability distribution, *GEOPHYSICS*, **76**(3), R43–R55.
- 400 Balmino, G., Vales, N., Bonvalot, S., & Briais, A., 2012. Spherical harmonic modelling to ultra high degree  
401 of Bouguer and isostatic anomalies, *Journal of Geodesy*, **86**(7), 499–520.
- 402 Beller, S., Monteiller, V., Operto, S., Nolet, G., Paul, A., & Zhao, L., 2017. Lithospheric architecture of the  
403 South-Western Alps revealed by multiparameter teleseismic full-waveform inversion, *Geophysical Journal  
404 International*, **212**(2), 1369–1388.
- 405 Bijani, R., Lelievre, P. G., Ponte-Neto, C. F., & Farquharson, C. G., 2017. Physical-property-, lithology-  
406 and surface-geometry-based joint inversion using Pareto Multi-Objective Global Optimization, *Geophysical  
407 Journal International*, **209**(2), 730–748.
- 408 Blom, N., Boehm, C., & Fichtner, A., 2017. Synthetic inversions for density using seismic and gravity data,  
409 *Geophysical Journal International*, **209**(2), 1204–1220.
- 410 Brocher, T., 2005. Empirical relations between elastic wavespeeds and density in the Earth’s crust, *Bull.  
411 Seismol. Soc. Am.*, **95**(6), 2081–2092.
- 412 Brown, V., K.-K. & Singh, S., 2012. Seismically regularized controlled-source electromagnetic inversion,  
413 *Geophysics*, **77**(1), E57–E65.
- 414 Chevrot, S., Villaseñor, A., Sylvander, M., & the PYROPE Team, 2014. High-resolution imaging of the  
415 Pyrenees and Massif Central from the data of the PYROPE and IBERARRAY portable array deployments,  
416 *J. Geophys. Res.*, **119**(8), 6399–6420.
- 417 Chevrot, S., Sylvander, M., Diaz, J., Ruiz, M., Paul, A., & the PYROPE Working group, 2015. The Pyrenean  
418 architecture as revealed by teleseismic P-to-S converted waves recorded along two dense transects, *Geophys.  
419 J. Int.*, **200**, 1096–1107.
- 420 Chevrot, S., Sylvander, M., Diaz, J., Martin, R., Mouthereau, F., Manatschal, G., Masini, E., Calassou, S., Gri-  
421 maud, F., Pauchet, H., & Ruiz, M., 2018. The non-cylindrical crustal architecture of the Pyrenees, *Scientific  
422 Reports*, **8**.
- 423 Colombo, D. & Stefano, M. D., 2007. Geophysical modeling via simultaneous joint inversion of seismic,  
424 gravity, and electromagnetic data: Application to prestack depth imaging, *The Leading Edge*, **26**(3), 326–  
425 331.
- 426 Darijani, M., Farquharson, C. G., & Lelièvre, P. G., 2020. Clustering and constrained inversion of seismic  
427 refraction and gravity data for overburden stripping: Application to uranium exploration in the athabasca  
428 basin, canada, *GEOPHYSICS*, **85**(4), B133–B146.
- 429 Gallardo, L. A. & Meju, M. A., 2003. Characterization of heterogeneous near-surface materials by joint 2d  
430 inversion of dc resistivity and seismic data, *Geophysical Research Letters*, **30**(13).
- 431 Geodesist’s-Handbook, 2012. The International Gravimetric Bureau, *Journal of Geodesy*, **86**(10), 946–949.
- 432 Giraud, J., Lindsay, M., Ogarko, V., Jessell, M., Martin, R., & Pakyuz-Charrier, E., 2019a. Integration of  
433 geoscientific uncertainty into geophysical inversion by means of local gradient regularization, *Solid Earth*,

- 434 **10**(1), 193–210.
- 435 Giraud, J., Ogarko, V., Lindsay, M., Pakyuz-Charrier, E., Jessell, M., & Martin, R., 2019b. Sensitivity of  
436 constrained joint inversions to geological and petrophysical input data uncertainties with posterior geological  
437 analysis, *Geophysical Journal International*, **218**(1), 666–688.
- 438 Grandjean, G., 1994. Étude des structures crustales dans une portion de chaîne et de leurs relations avec les  
439 bassins sédimentaires, application aux Pyrénées occidentales, *Bull. Centre Rech. Expl. Prod. Elf-Aquitaine*,  
440 **18**, 391–419.
- 441 Gómez-Romeu, J., Masini, E., Tugend, J., Ducoux, M., & Kuszniir, N., 2019. Role of rift structural inheritance  
442 in orogeny highlighted by the western pyrenees case-study, *Tectonophysics*, **766**, 131 – 150.
- 443 Herceg, M., Artemieva, I., & Thybo, H., 2015. Sensitivity analysis of crustal correction for calculation of  
444 lithospheric mantle density from gravity data, *Geophysical Journal International*, **204**(2), 687–696.
- 445 Lelievre, P. G., Farquharson, C. G., & Hurich, C. A., 2012. Joint inversion of seismic traveltimes and gravity  
446 data on unstructured grids with application to mineral exploration, *GEOPHYSICS*, **77**(1), K1–K15.
- 447 Lescoutre, R., 2019. *Formation et réactivation du système de rift pyrénéo-cantabrique : héritage, segmentation*  
448 *et évolution thermique*, Ph.D. thesis, Ecole et Observatoire des Sciences de la Terre, Université de Strasbourg.
- 449 Lescoutre, R. & Manatschal, G., 2020. Role of rift-inheritance and segmentation for orogenic evolution:  
450 example from the Pyrenean-Cantabrian system, *BSGF - Earth Sci. Bull.*, **191**, 18.
- 451 Lin, W. & Zhdanov, M. S., 2019. The gramian method of joint inversion of the gravity gradiometry and seismic  
452 data, *Pure and Applied Geophysics*, **176**(4), 1659–1672.
- 453 Lines, L., 1999. Density and AVO, *Canadian journal of exploration geophysics*, **35**(1/2), 32–35.
- 454 Ludwig, W., Nafe, J., & Drake, C., 1970. *Seismic Refraction, the Sea*, vol. 4, Wiley-Interscience, A. E. Maxwell  
455 ed., New-York, USA.
- 456 Martin, R., Monteiller, V., Komatitsch, D., Perrouty, S., Jessell, M., Bonvalot, S., & Lindsay, M., 2013. Gravity  
457 inversion using wavelet-based compression on parallel hybrid CPU/GPU systems: Application to southwest  
458 Ghana, *Geophysical Journal International*, **195**(3), 1594–1619.
- 459 Martin, R., Chevrot, S., Komatitsch, D., Seoane, L., Spangenberg, H., Wang, Y., Dufrécho, G., Bonvalot, S.,  
460 & Bruinsma, S., 2017. A high-order 3-D spectral-element method for the forward modelling and inversion of  
461 gravimetric data - Application to the western pyrenees, *Geophysical Journal International*, **209**(1), 406–424.
- 462 Martin, R., Ogarko, V., Komatitsch, D., & Jessell, M., 2018. Parallel three-dimensional electrical capacitance  
463 data imaging using a nonlinear inversion algorithm and Lp norm-based model regularization, *Measurement*,  
464 **128**, 428 – 445.
- 465 Meju, M. A. & Gallardo, L. A., 2016. *Structural Coupling Approaches in Integrated Geophysical Imaging*,  
466 chap. 4, pp. 49–67, American Geophysical Union (AGU).
- 467 Monteiller, V., Chevrot, S., Komatitsch, D., & Fuji, N., 2013. A hybrid method to compute short-period  
468 synthetic seismograms of teleseismic body waves in a 3-D regional model, *Geophys. J. Int.*, **192**, 230–247.
- 469 Monteiller, V., Chevrot, S., Komatitsch, D., & Wang, Y., 2015. Three-dimensional full waveform inversion of  
470 short-period teleseismic wavefields based upon the SEM-DSM hybrid method, *Geophys. J. Int.*, **202**, 811–

- 471 827.
- 472 Moorkamp, M., Heincke, B., Jegen, M., Roberts, A., & Hobbs, R., 2011. A framework for 3-D joint inversion  
473 of MT, gravity and seismic refraction data, *Geophysical Journal International*, **184**(1), 477–493.
- 474 Nafe, J. E. & Drake, C. L., 1957. Variation with depth in shallow and deep water marine sediments of porosity,  
475 density and the velocities of compressional and shear waves, *GEOPHYSICS*, **22**(3), 523–552.
- 476 Paige, C. C. & Saunders, M. A., 1982. LSQR: An algorithm for sparse linear equations and sparse least  
477 squares, *ACM Trans. Math. Softw.*, **8**(1), 43–71.
- 478 Portniaguine, O. & Zhdanov, M. S., 2002. 3-D magnetic inversion with data compression and image focusing,  
479 *GEOPHYSICS*, **67**(5), 1532–1541.
- 480 Saunders, J. H., Herwanger, J. V., Pain, C. C., Worthington, M. H., & De Oliveira, C. R. E., 2005. Constrained  
481 resistivity inversion using seismic data, *Geophysical Journal International*, **160**(3), 785–796.
- 482 Souriau, A. & Pauchet, H., 1998. A new synthesis of pyrenean seismicity and its tectonic implications,  
483 *Tectonophysics*, **290**(3), 221 – 244.
- 484 Stefano, M. D., Andreasi, F. G., Re, S., Virgilio, M., & Snyder, F. F., 2011. Multiple-domain, simultaneous  
485 joint inversion of geophysical data with application to subsalt imaging, *GEOPHYSICS*, **76**(3), R69–R80.
- 486 Tarantola, A. & Valette, B., 1982a. Generalized nonlinear inverse problems solved using the least squares  
487 criterion, *Rev. Geophys. Space Phys.*, **20**, 219–232.
- 488 Tarantola, A. & Valette, B., 1982b. Inverse problem = quest for information, *J. Geophysics*, **50**, 159–170.
- 489 Virieux, J. & Operto, S., 2009. An overview of full-waveform inversion in exploration geophysics, *Geophysics*,  
490 **74**(6), WCC1–WCC26.
- 491 Wang, Y., Chevrot, S., Monteiller, V., Komatitsch, D., Mouthereau, F., Manatschal, G., Sylvander, M., Diaz,  
492 J., Ruiz, M., Grimaud, F., Benahmed, S., Pauchet, H., & Martin, R., 2016. The deep roots of the western  
493 Pyrenees revealed by full waveform inversion of teleseismic P-waves, *Geology*, **44**(6), 475–478.
- 494 Wehr, H., Chevrot, S., Courrioux, G., & Guillen, A., 2018. A three-dimensional model of the pyrenees and  
495 their foreland basins from geological and gravimetric data, *Tectonophysics*, **734-735**, 16 – 32.
- 496 Welford, J. K., Peace, A. L., Geng, M., Dehler, S. A., & Dickie, K., 2018. Crustal structure of Baffin Bay from  
497 constrained three-dimensional gravity inversion and deformable plate tectonic models, *Geophysical Journal  
498 International*, **214**(2), 1281–1300.
- 499 Yan, P., K. T. H. P. & Garcia Juanatey, M. A., 2017. Two-dimensional magnetotelluric inversion using reflec-  
500 tion seismic data as constraints and application in the COSC project, *Geophysical Research Letters*, **44**(8),  
501 3554–3563.

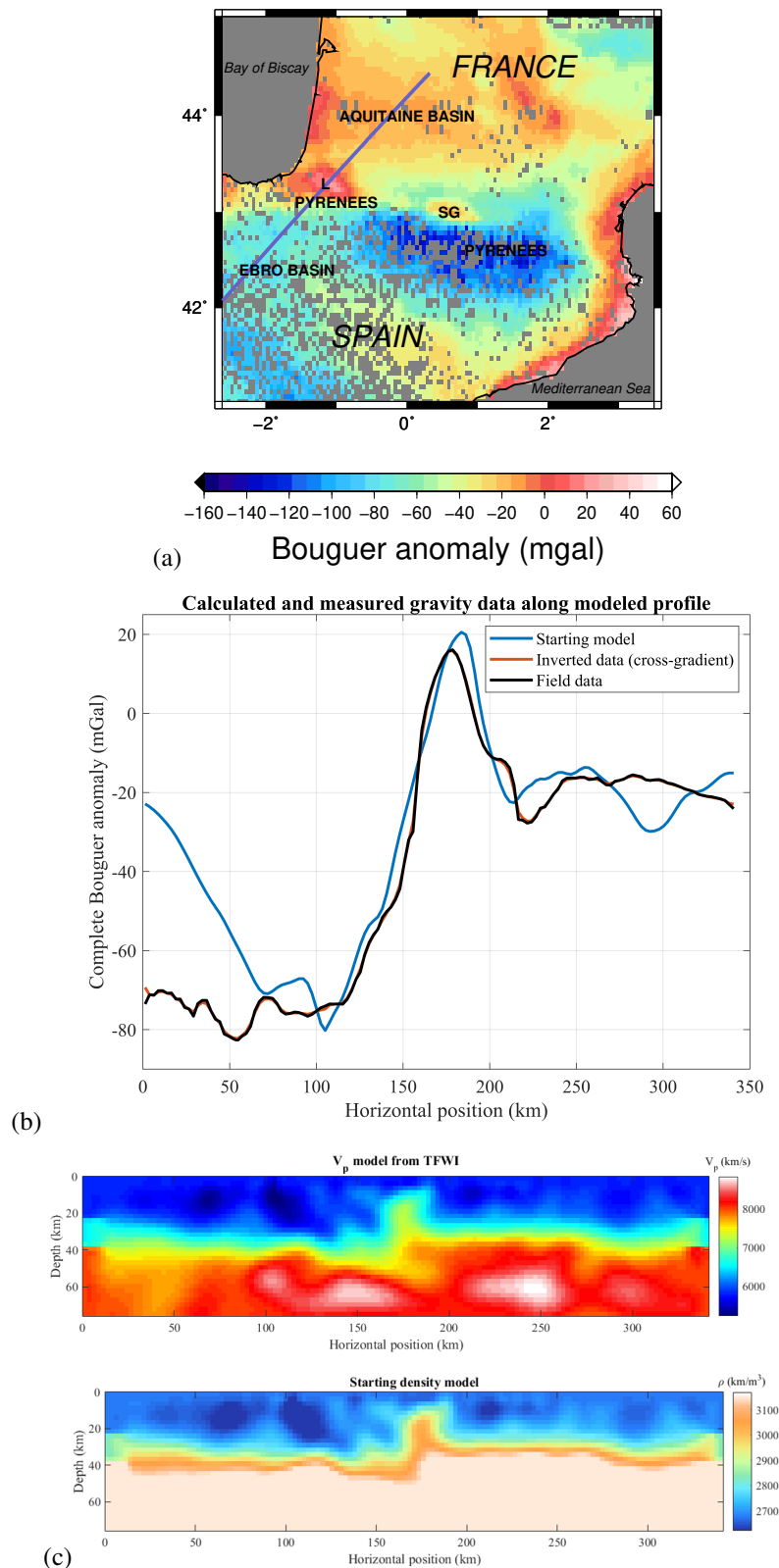


**Figure 1.** (a) Measured Bouguer gravity anomaly data in Southwest France and North Spain. The western transect seismic profile A-A' crossing the Mauleon and Ebro basin in the Pyrenees close to Labour town (Chevrot et al. 2018) is shown in blue. (b-middle) Observed (black solid) and a priori (blue solid) Bouguer gravity anomalies close to the westernmost transect A-A'. (c)  $V_p$  and Nafe-Drake scaled prior density model  $\rho$  along the A-A' profile.

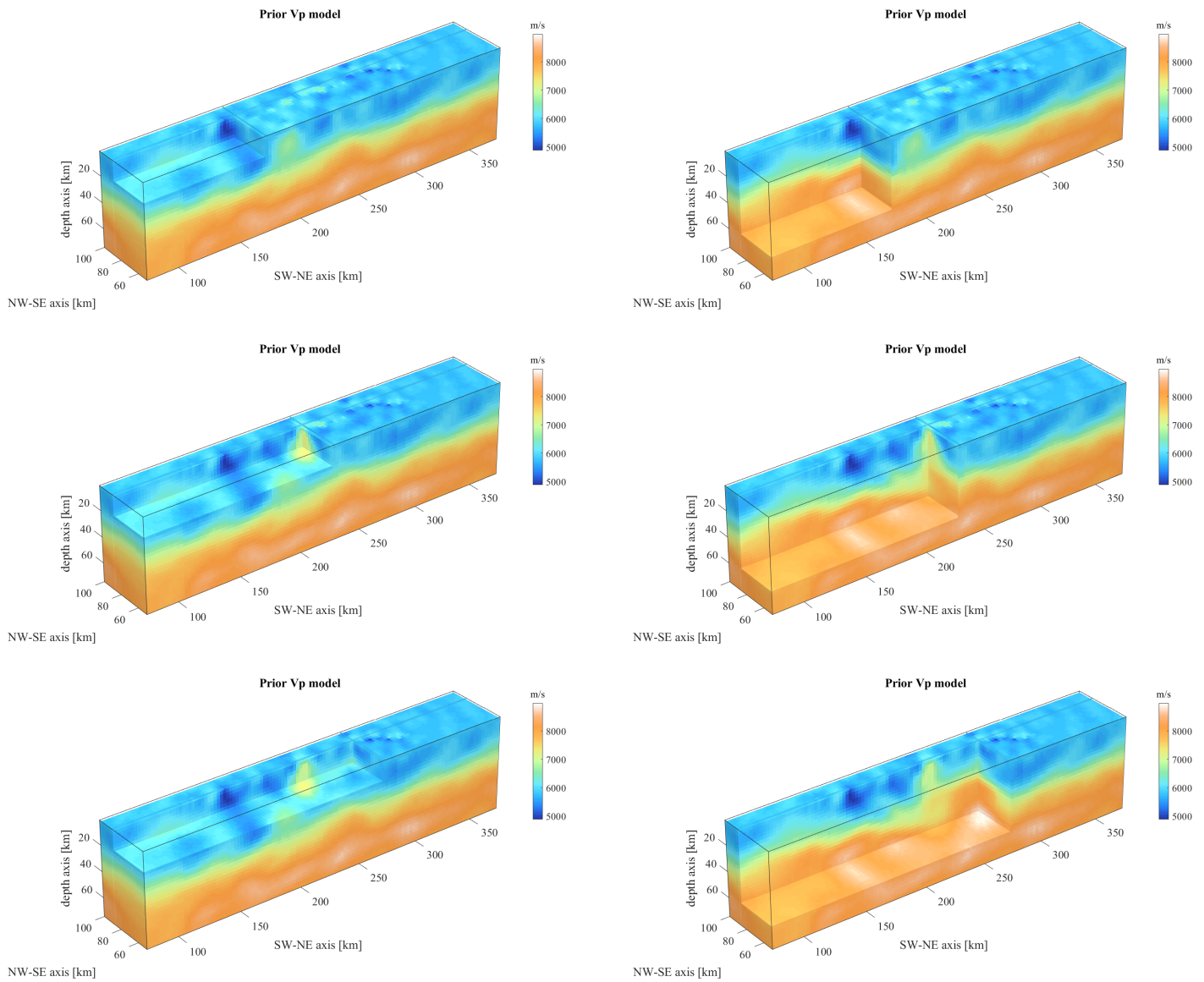


**Figure 2.** 3D  $V_p$  model along the A-A' profile at 16.4 km (left column) and 50 km depth (right column). Sections perpendicular to the A-A' profile are shown too at  $x = 200$  km (top), 226 km (middle, where the exhumed mantle is going up close to the surface) and 290 km.

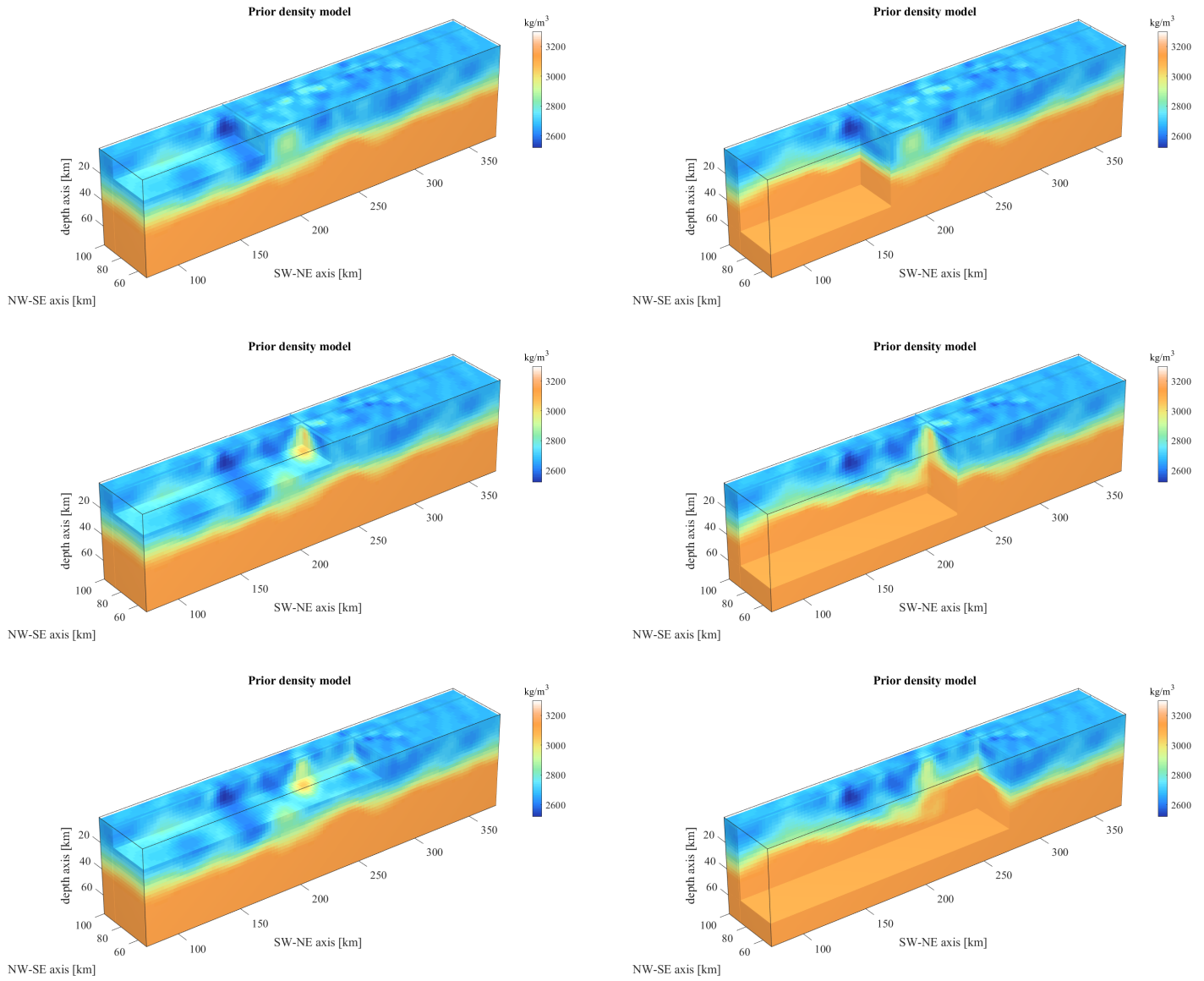


**Figure 3.** 3D Nafe-Drake scaled prior density model  $\rho$  along the A-A' profile at 16.4 km (left column) and 50 km depth (right column). Sections perpendicular to the A-A' profile are shown too at  $x = 200$  km (top), 226 km (middle, where the exhumed mantle is going up close to the surface) and 290 km.

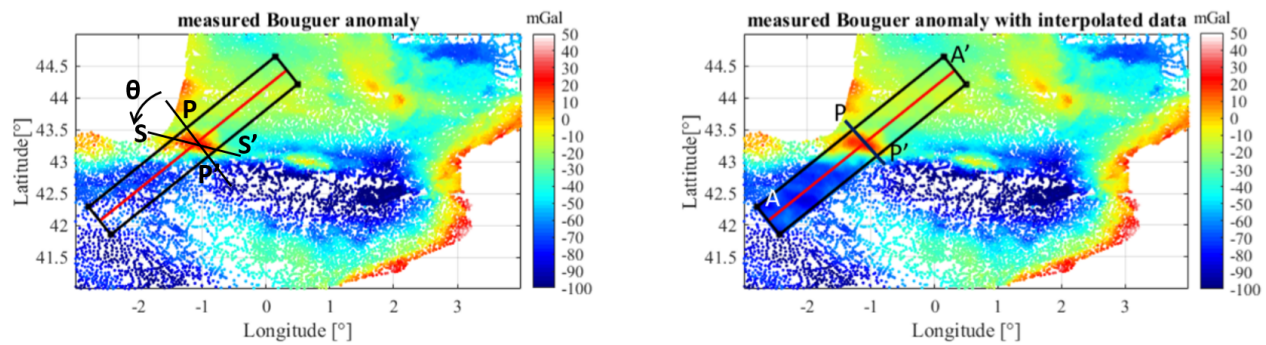


**Figure 4.** Top view of the measured/not gridded data is shown (left) as well as the data interpolated (right) in the region of interest (inside the black box) containing the (A-A') seismic profile (red line). The interpolated data are gridded at 2.471 km resolution. The line segment P-P' perpendicular to the seismic profile and the Pyrenean strike segment S-S' passing through the Mauleon's gravity anomaly are shown. Both segments make an angle  $\theta$  around 40 degrees.

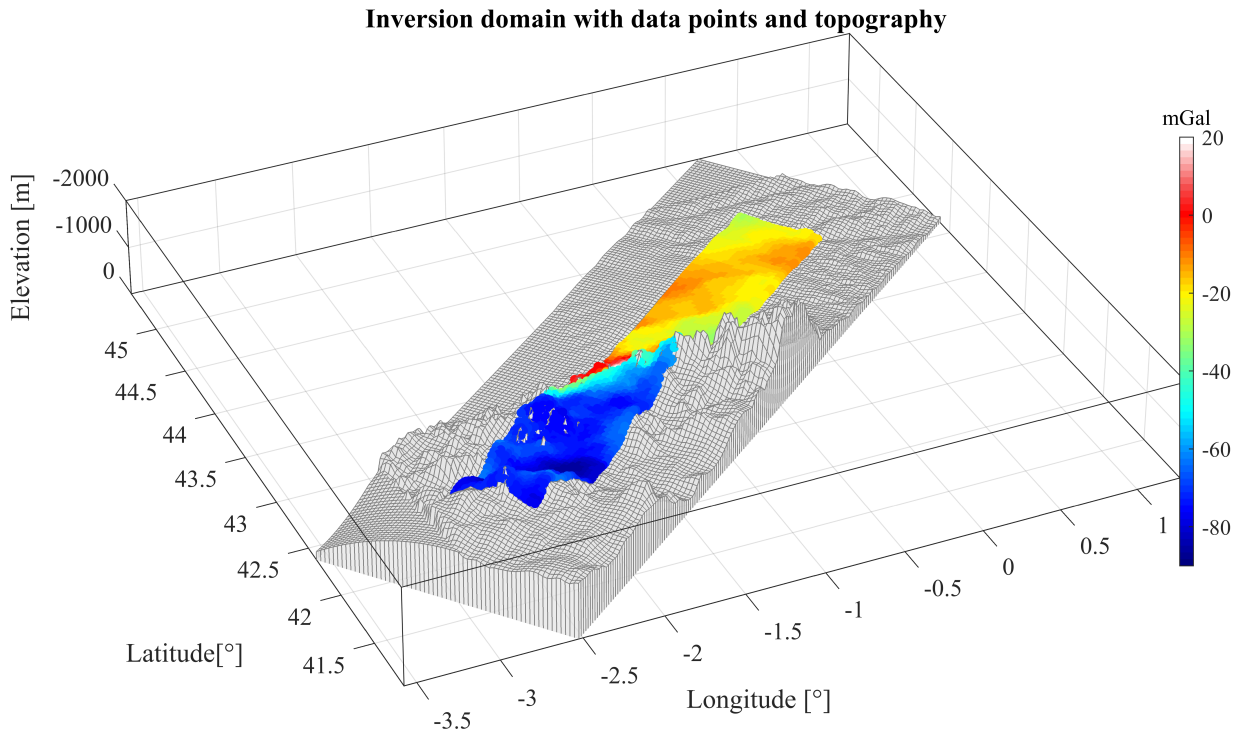


**Figure 5.** Bouguer gravity anomaly interpolated on the topography in the computational slice of interest. ETOPO1 1 mn arc resolution topography interpolated at 2.471 km resolution is considered in the computational area of interest that includes the (A-A') seismic profile. The computational mesh used for data inversion takes into account the topography. The first layer of the computational mesh is distorted, follows the topography and is also shown on the figure. Lateral padding of the computational model is added, taking into account the topography outside the set of gravity data (in color).

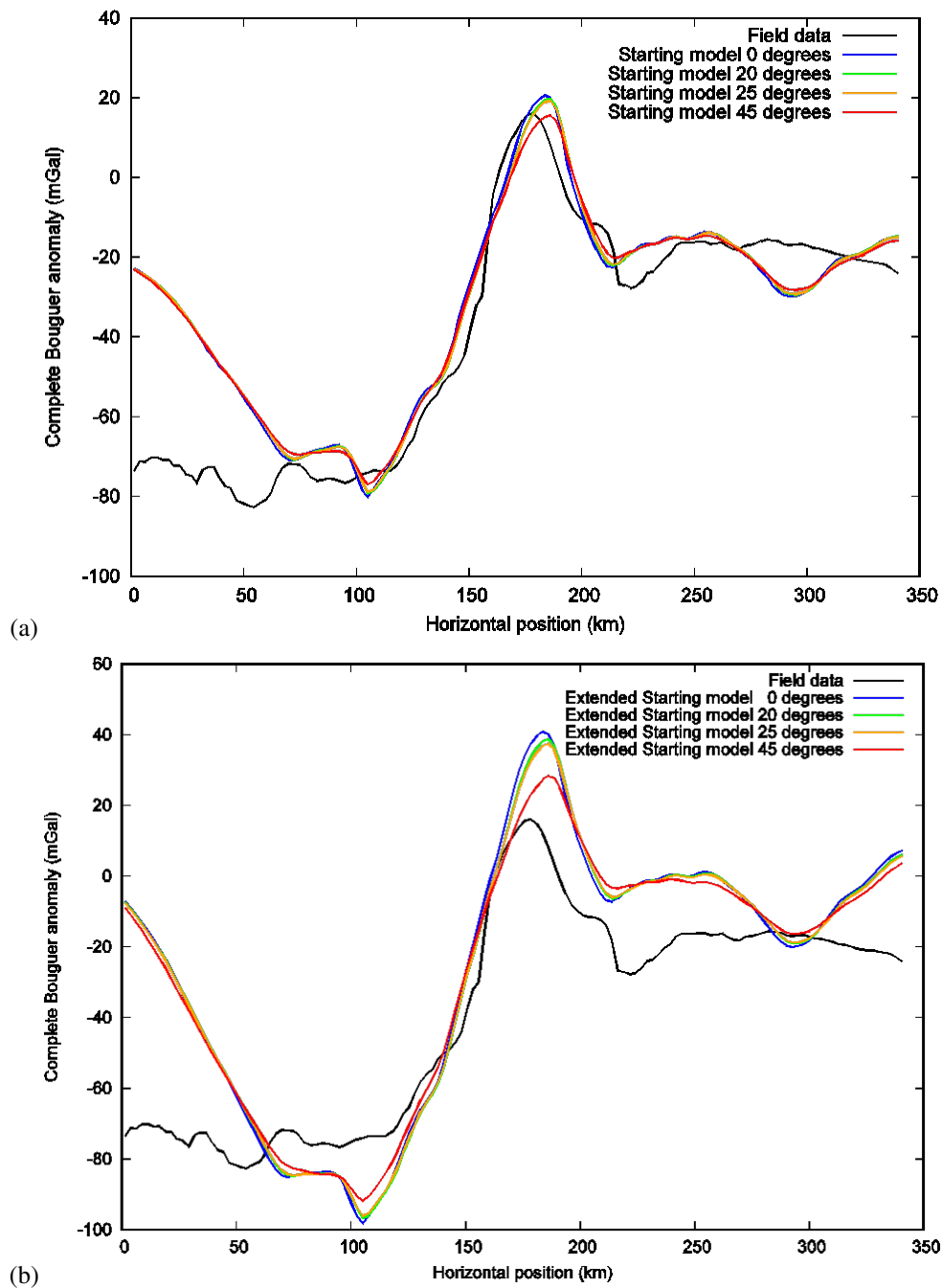


**Figure 6.** (a) Bouguer gravity anomalies are shown for the a priori 2.5D model extracted from the 3D TFWI model, interpolated at 2.471 km resolution along the (A-A') seismic profile and replicated invariantly to itself over a width of 30 km. Four cases are plotted : in the direction perpendicular to the profile (angle  $0^\circ$ ) or rotated by an angle ( $20^\circ$ ,  $25^\circ$ ,  $45^\circ$ ) respect to the profile. The a priori anomalies are very similar and are comparable to the observed field anomalies. (B) Same thing as in Figure A but for a 44 km width of the density anomalies. We can observe that the anomalies are overestimated when compared to the 30 km model width case with or without rotation of the model.

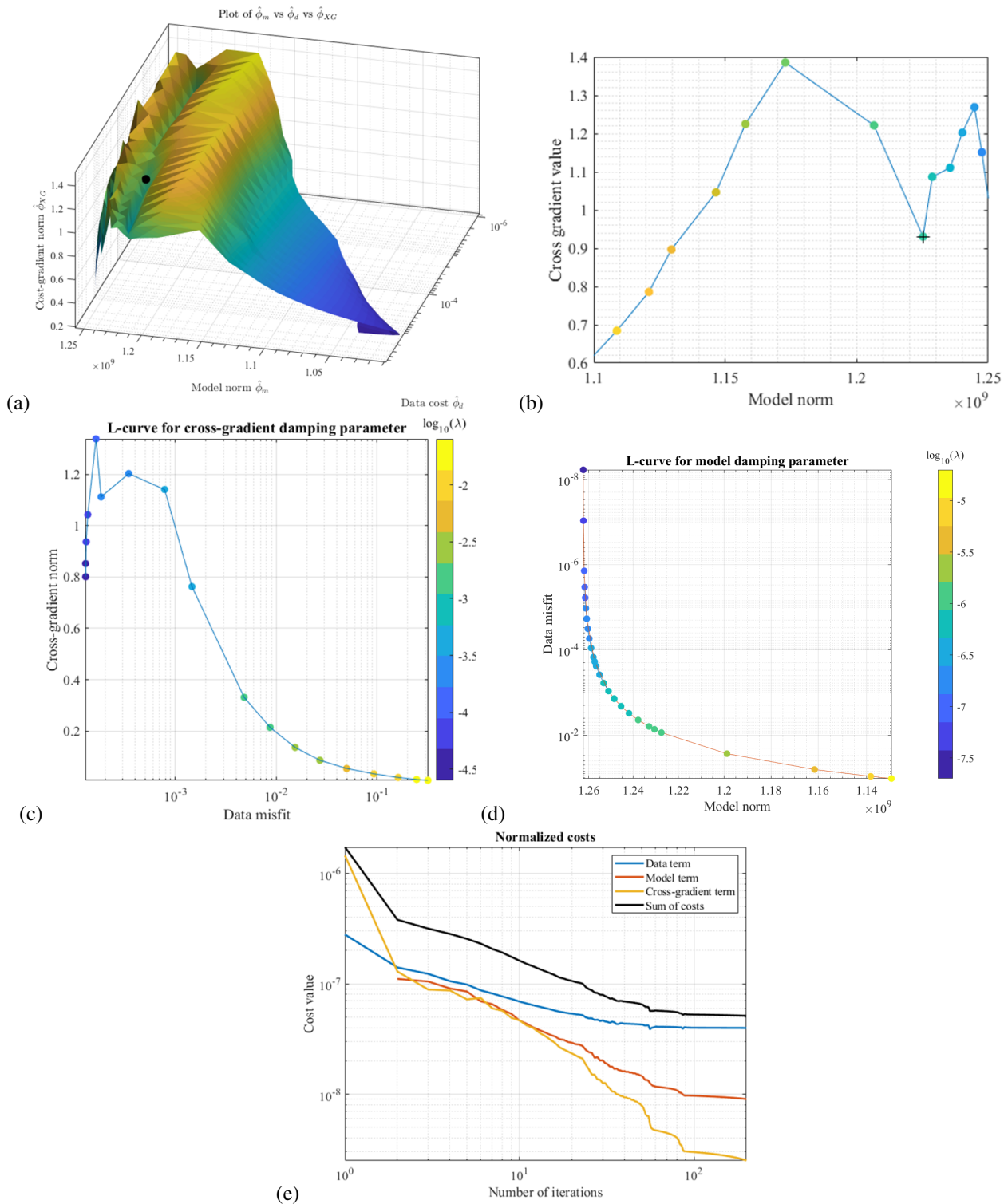


**Figure 7.** Data misfits are normalized by the sum of squared data. (a-Top) 3D representation of the three terms of the cost function. The optimal regularization parameters are indicated by the black dot. (b-Top) Section of this surface passing through this point. (c and d : Middle left and right)  $L$  curves to define the optimal model regularization and cross-gradient weights respectively corresponding to the optimal model damping and cross-gradient terms shown in Figure (a). Refined subrange of weighting parameters  $(\lambda, \alpha)$  varying in the set intervals  $[10^{-8}, 5 \cdot 10^{-5}] \times [10^{-5}, 10^{-1}]$  has been used. (e-Bottom) Evolution of data misfit, cross-gradient and model damping norms through inversion iterations.

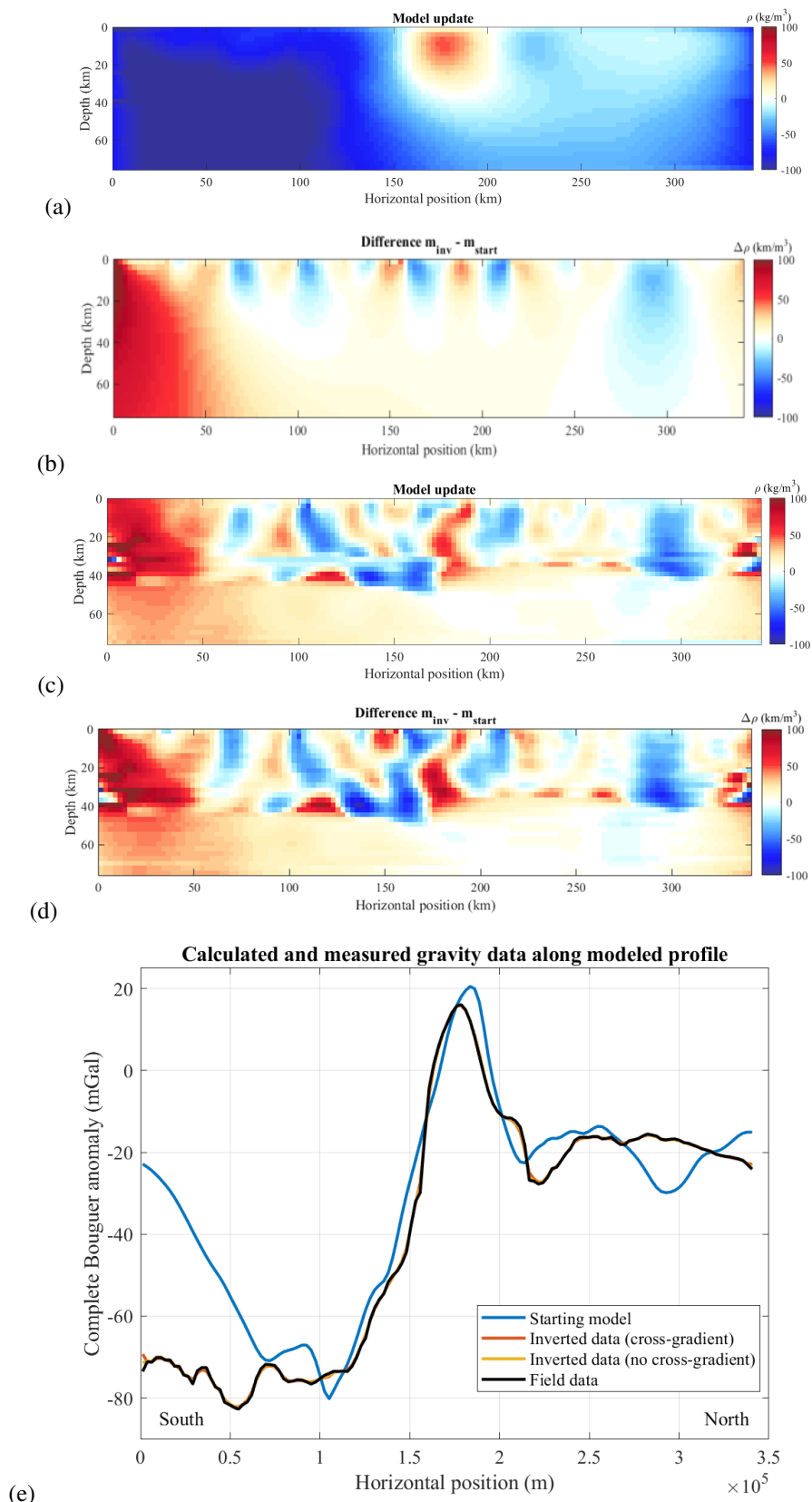


**Figure 8.** Difference between inverted and prior density models in the 2.5D ('quasi 3D') case. (Top) Without cross-gradient constraint, and without (a) or with (b) starting model. (Middle) With cross-gradient constraint, and without (c) or with (d) starting model. Strong differences are appearing at depth, with variations exceeding + or - 100  $\text{kg/m}^3$ , particularly when cross-gradient constraint is applied. Note also that differences are predominantly vertical. (Bottom-e) Observed and inverted gravity data with and without cross-gradient constraint.

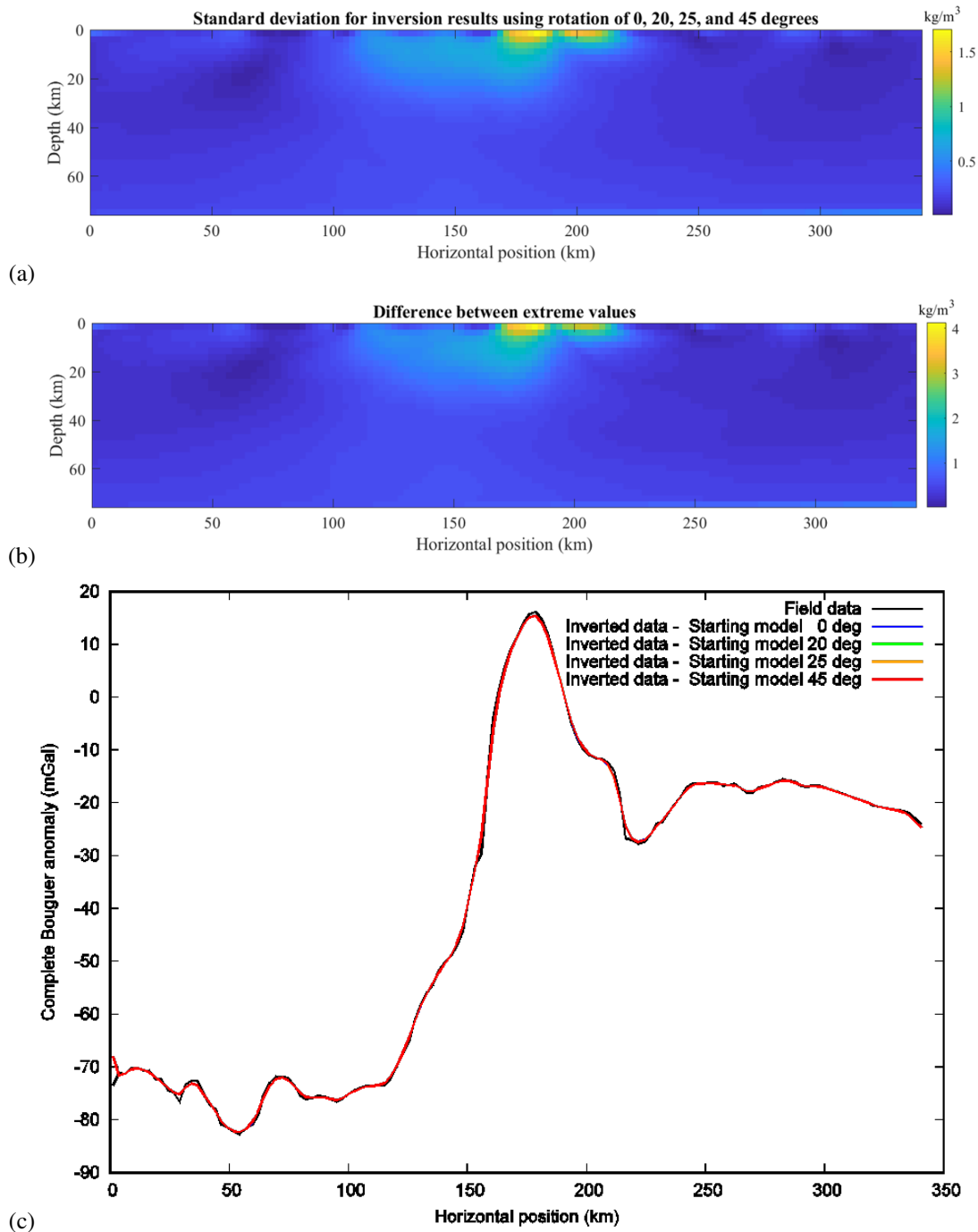


**Figure 9.** We show the standard deviation (Figure a) as well as the difference per cell between the maximum and minimum density values (Figure b) over all the four inverted models obtained for the prior models rotated by an angle of 0, 20, 25 and 45 degrees in the trigonometric sense respect to P-P' transect. Minimum and maximum values of + or - 4  $\text{kg/m}^3$ , and maximum standard deviations of around 1.7  $\text{kg/m}^3$  are reached. There is not any significant difference between the inverted models. In Figure c the inverted gravity data are shown for the four cases with the different angles : there is almost no differences between them.

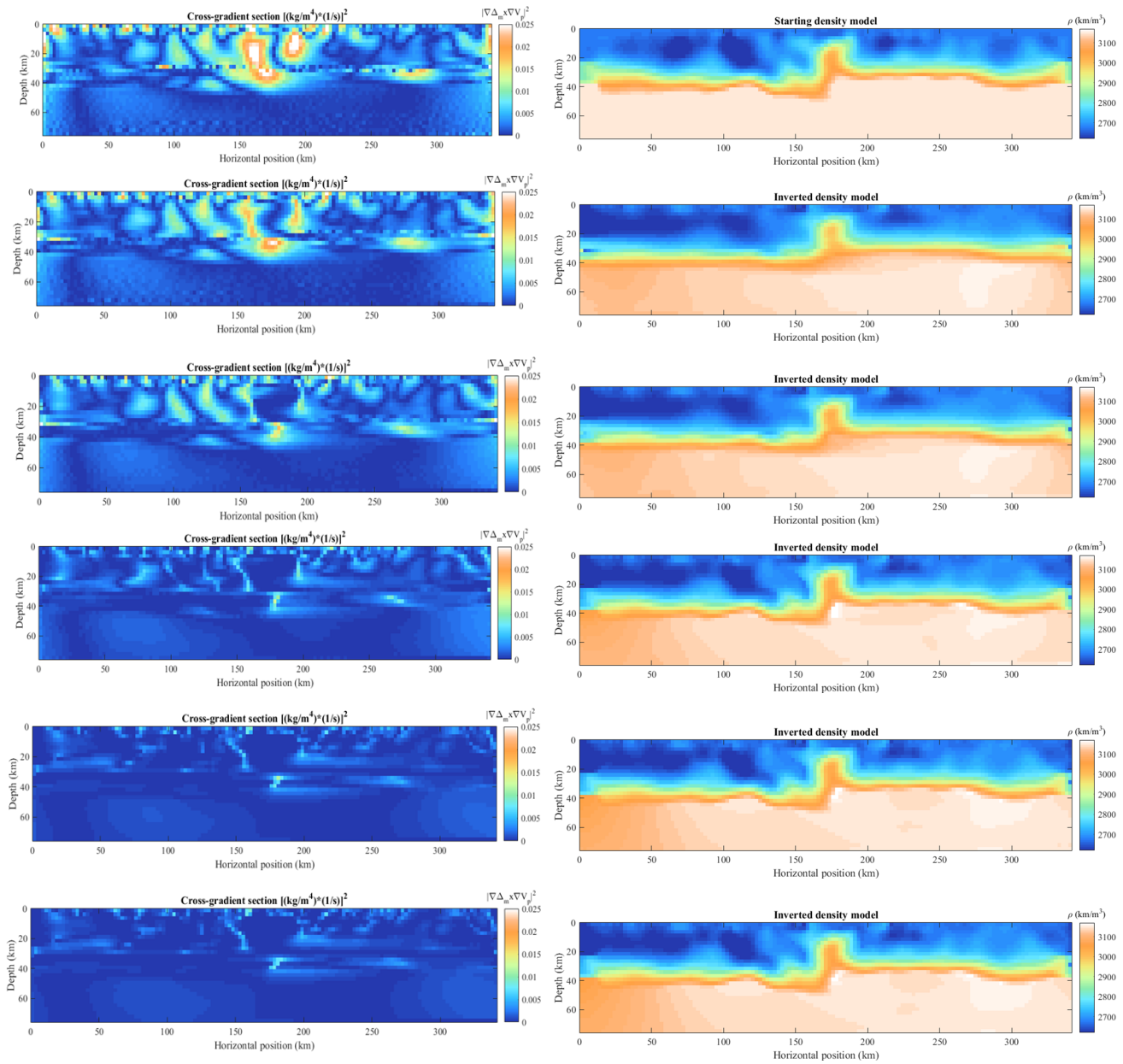


**Figure 10.** (Left) From top to bottom : cross-gradient evolution for 5, 10, 50, 100 and 200 inversion loops. Cross-gradient is decreasing as expected. (Right) Inverted effective densities with cross-gradient constraints.

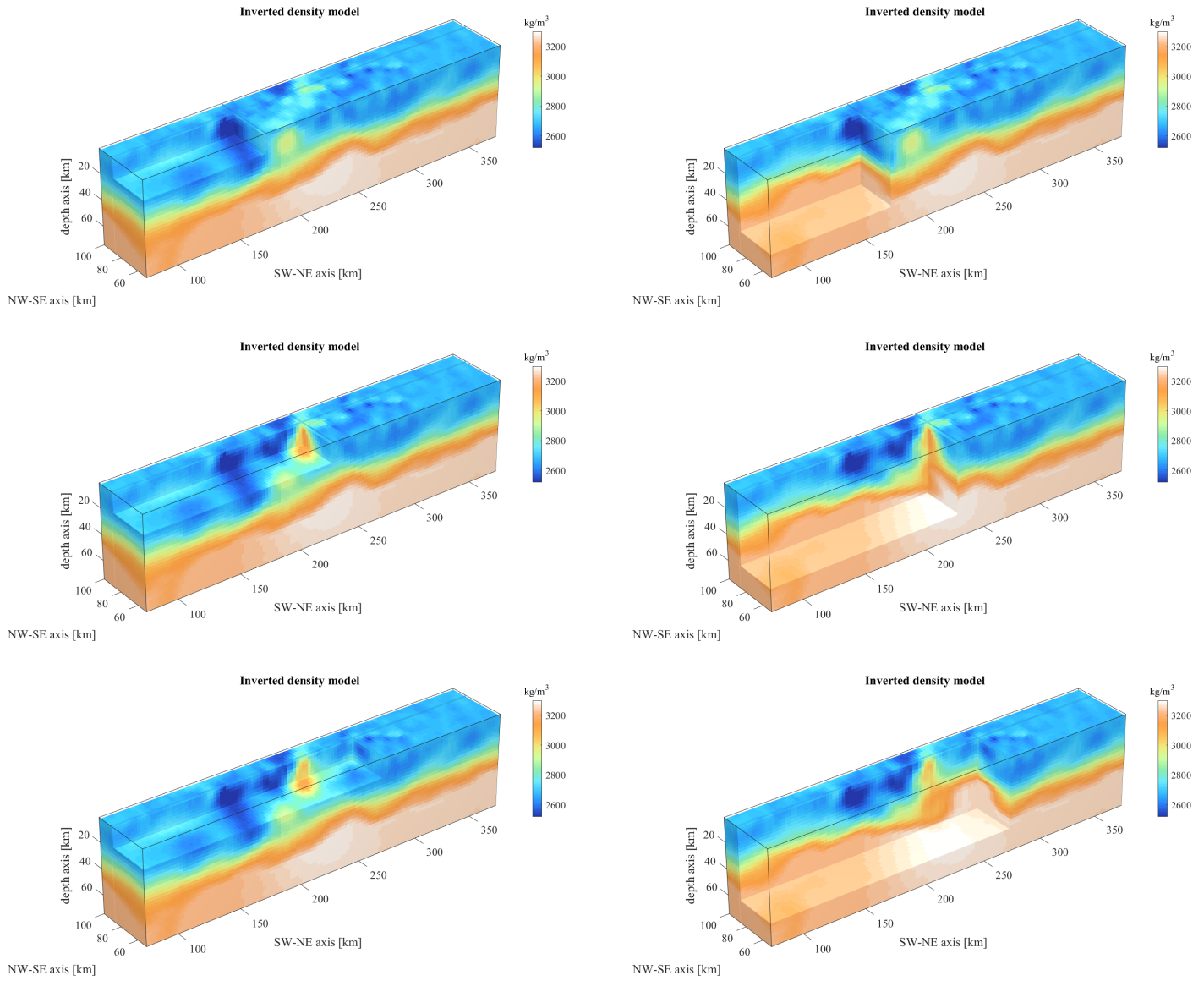


**Figure 11.** 3D inverted density model  $\rho$  along the A-A' profile at 16.4 km (left column) and 50 km depth (right column). Sections perpendicular to the A-A' profile are shown too at  $x = 200$  km (top), 226 km (middle, where the exhumed mantle is going up close to the surface) and 290 km.

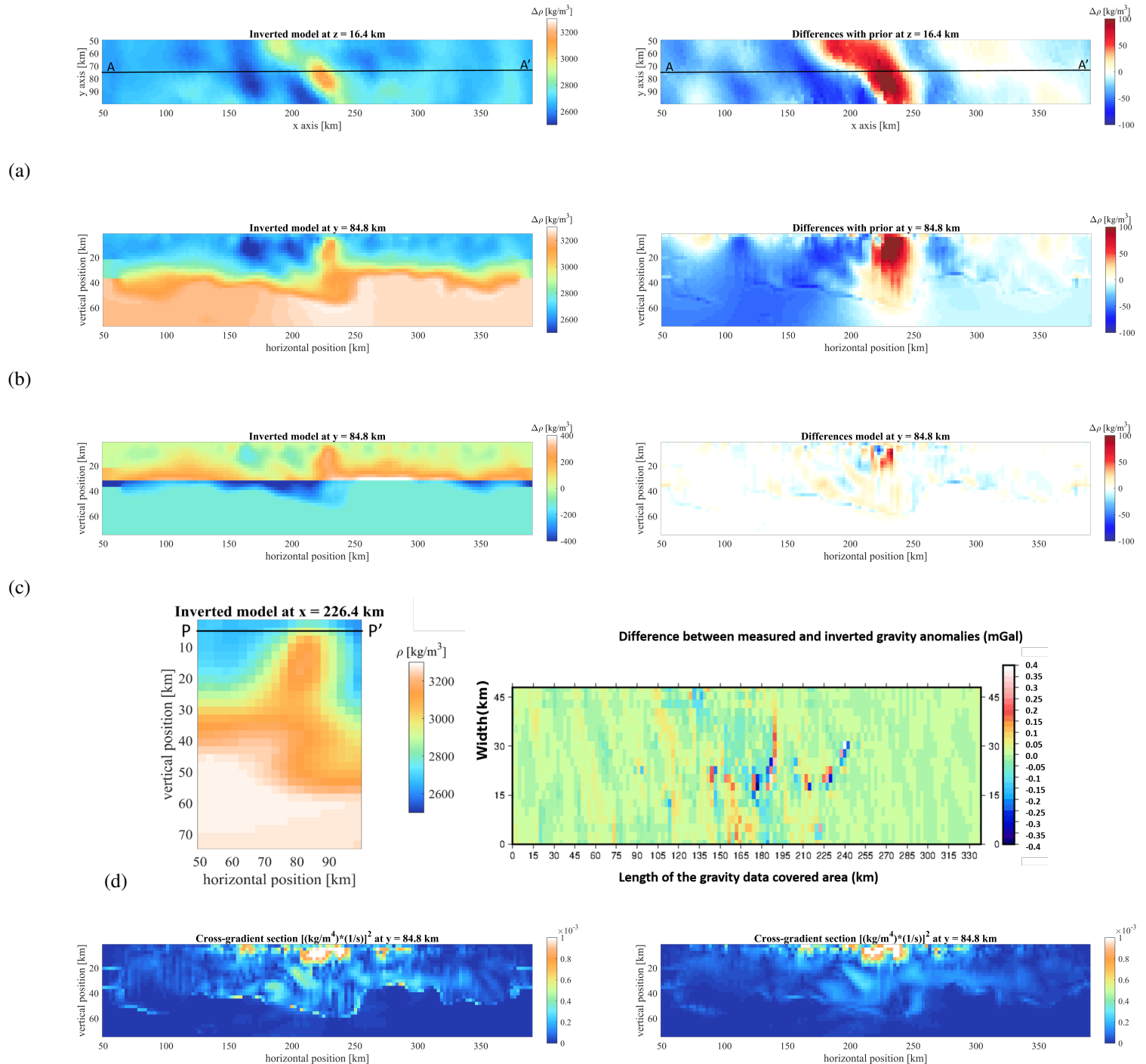


**Figure 12.** Full 3D gravity data inversion results. (a) Left: Density model along the (A-A') profile at 16.4 km depth. Right: Difference between inverted and prior Nafe-Drake scaled model. (b) Left: vertical inverted density model section along A-A' profile. Right: Difference between inverted and prior Nafe-Drake model. (c) Left: Vertical density anomaly section (relative to the 2670 kg/m<sup>3</sup> crust and 3270 kg/m<sup>3</sup> Moho density reference model) along A-A' profile. Right: Difference between inverted and starting model. (d) Left: Vertical inverted density section along the Pyrenean axis perpendicular to A-A' transect. Right : Observed and inverted gravity data differences (lower than 0.4 mGal) on topography. (e) Cross-gradient before (left) and after (right) inversion.

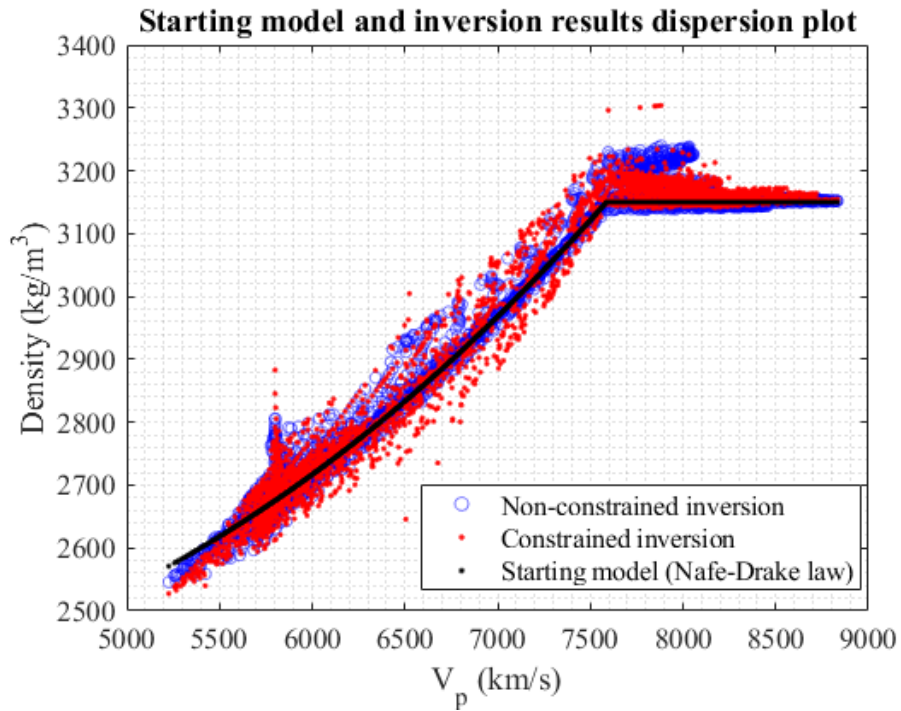


**Figure 13.** Dispersion diagram of  $\rho/V_p$  properties around the initial  $\rho/V_p$  Nafe-Drake scaling relation with and without seismic constraints. The correlation between inverted density and  $V_p$  models obtained after gravity data inversion constrained by seismics is shown in red (blue for the non-constrained inversion case). When compared to the non-constrained densities, the seismic constrained densities are lowered close to the surface and also at depth, in the northern part of the section and in the dipping part of the Iberian crust.

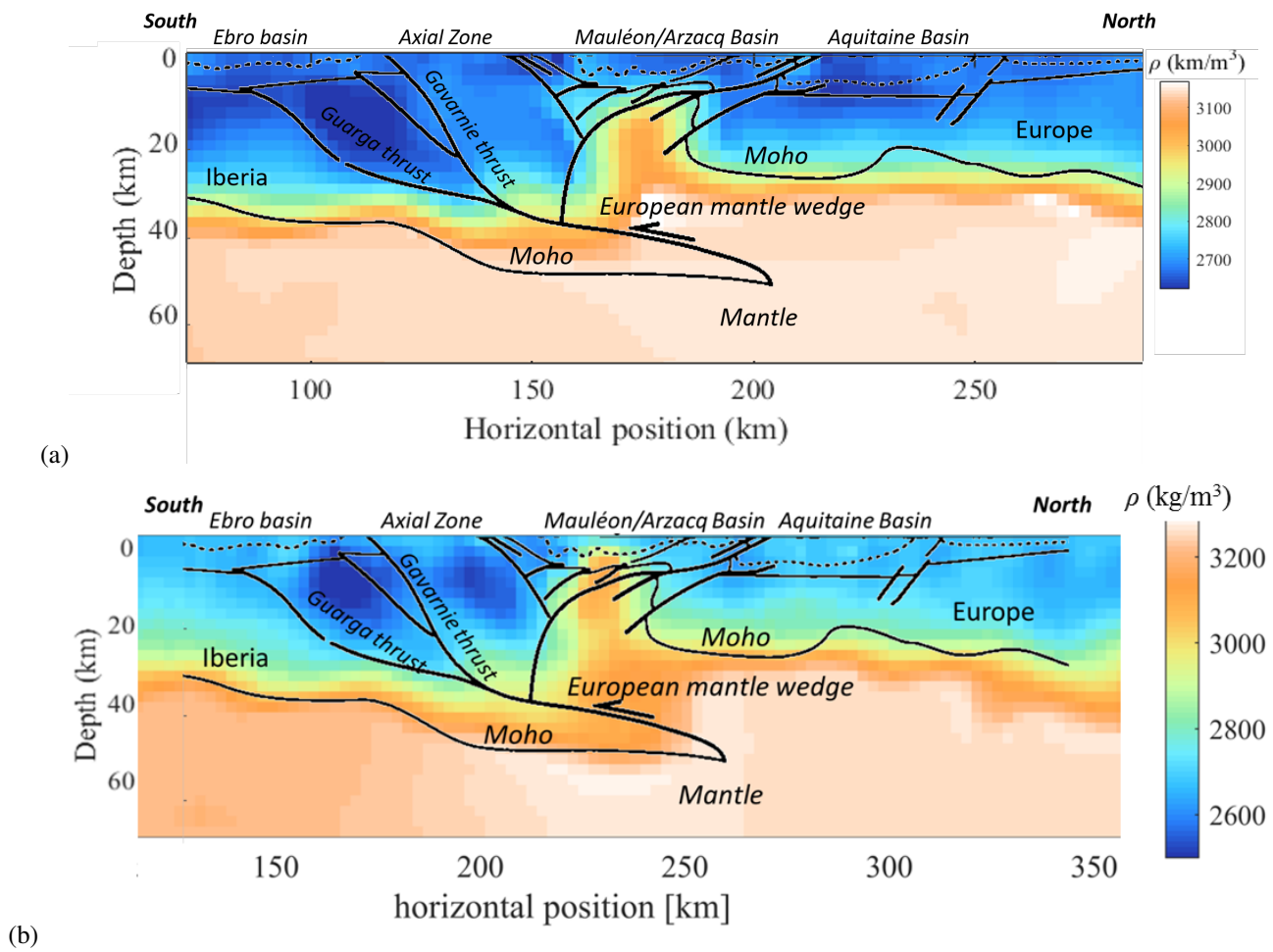


**Figure 14.** Zoomed density after inversion overlaid with geological interpretation of tomographic model from Wang et al. (2016) for the 2.5D case (Figure a) and the full 3D case (Figure b)

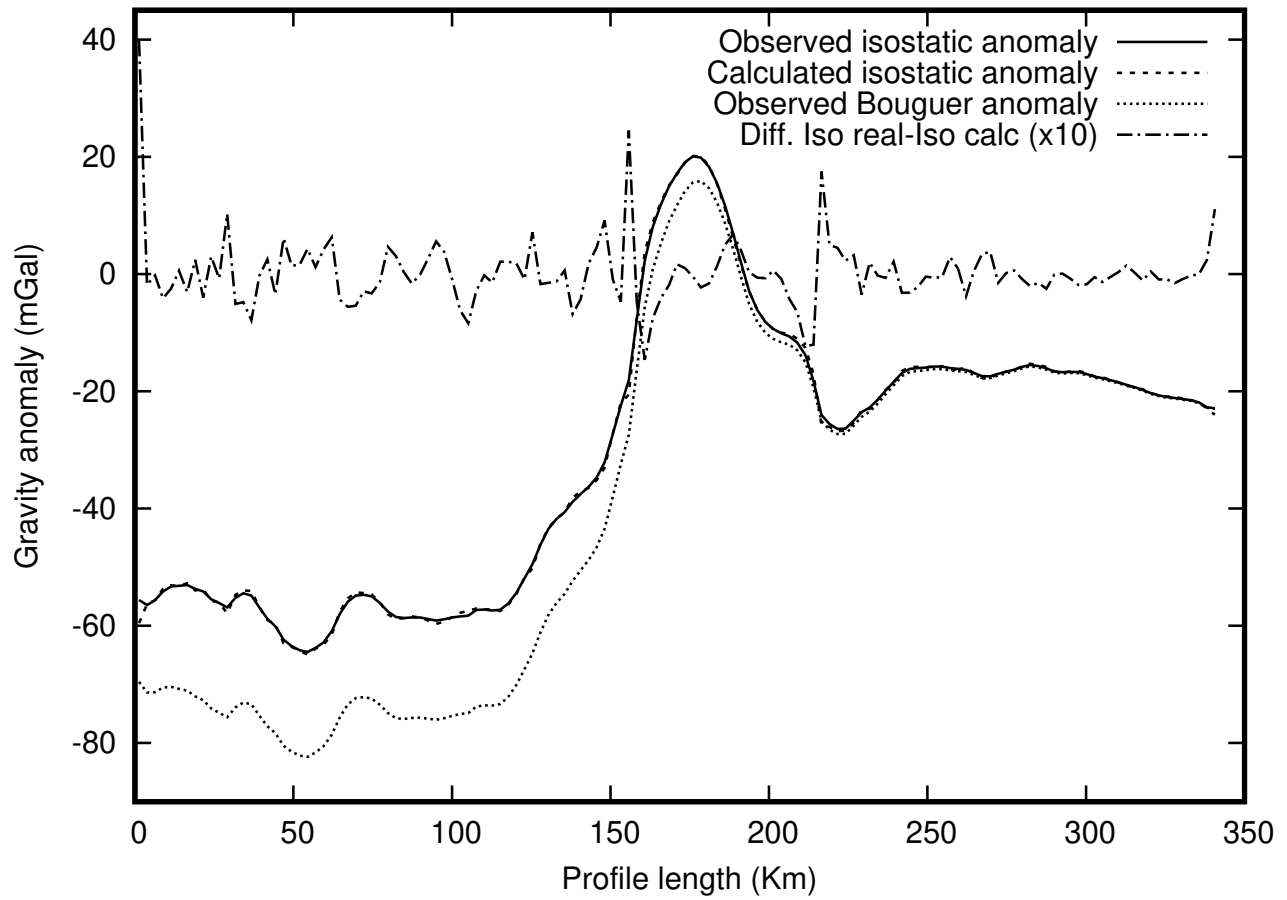


**Figure 15.** Difference between observed and computed (after inversion) isostatic anomalies for a reference Moho computed with a 30 km compensation depth.

502 **APPENDIX A: INVERSION ALGORITHM**

503 A least-squares algorithm is used here to solve the matrix system as follows. Let us denote  $m$  the  
 504 model vector containing the density anomalies  $\Delta\rho$ . This model vector is obtained by solving the  
 505 linear system of equation

$$\begin{bmatrix} SW^{-1} \\ \lambda I_d \\ \alpha W^{-1} \nabla V_p \wedge \nabla \end{bmatrix} [Wm] = \begin{bmatrix} \Delta g_{obs} \\ \lambda W m_p \\ 0 \end{bmatrix}, \quad (\text{A.1})$$

506 where  $m_p = \Delta\rho_p$  is the a priori model and the gravity kernel  $S$  is depth-weighted by the operator  
 507  $W$  given in equation (4). The solution of (A.1) is obtained by an iterative LSQR algorithm (Paige &  
 508 Saunders 1982). At each  $i$ -th LSQR inversion cycle we solve the following linearized version of the  
 509 system of equations (A.1)

$$\begin{array}{l} \text{For } 1 \leq i \leq Niter_{max} \\ \begin{bmatrix} SW^{-1} \\ \lambda I_d \\ \alpha W^{-1} \nabla V_p \wedge \nabla \end{bmatrix} [\Delta \bar{m}^i] = \begin{bmatrix} \Delta g_{obs} - \Delta g(m^{i-1}) \\ -\lambda W(m^{i-1} - m_p) \\ -\alpha \nabla V_p \wedge \nabla m^{i-1} \end{bmatrix} \\ \Delta m^i = W^{-1} \Delta \bar{m}^i \\ m^i = m^{i-1} + \Delta m^i \\ \text{End for} \end{array}, \quad (\text{A.2})$$

510 where  $Niter_{max}$  is the maximum number of outer loop inversion cycles. Spatial gradients are  
 511 computed using forward finite difference integration in the computation domain and using backward  
 512 finite difference integration at the outer boundaries.

513 **APPENDIX B: INFLUENCE OF INITIAL MODELS AND PENALTY CONSTRAINTS ON**  
 514 **DENSITY MODEL RECONSTRUCTION : DATA AND MODELS WITH OR WITHOUT**  
 515 **STARTING MODELS, DAMPING REGULARIZATION AND CROSS-GRADIENT**  
 516 **CONSTRAINTS.**

517 Let us first consider the impact of an a priori model, a damping term on the model or a cross-gradient  
 518 in the misfit function. As an example we consider the 2.5D model case (i.e for a 2D model defined as  
 519 a Nafe-Drake scaled density model and extrapolated in the direction orthogonal to the A-A' profile).  
 520 As shown in Figures A2, the data misfit function is well minimized in all cases, which suggests that  
 521 the solution of the inverse problem is not unique. Figure A3 shows the effective density models and

522 the difference with the a priori model (scaled from the  $V_p$  model using a Nafe-Drake law) or a density  
 523 model of reference. In Figures 8 and A3, the inverted solutions are represented for inversions with  
 524 and without starting models in the following cases :

- 525 • Case 1 : without damping ( $\lambda = 0$ ) and without cross-gradient ( $\alpha = 0$ )
- 526 • Case 2 : with damping ( $\lambda \neq 0$ ) and without cross-gradient ( $\alpha = 0$ )
- 527 • Case 3 : without damping ( $\lambda = 0$ ) and with cross-gradient ( $\alpha \neq 0$ )

528 where the non zero parameters  $\lambda$  (case 2) and  $\alpha$  (case 3) are chosen for clarity as the optimal values  
 529 ( $\lambda = 5 \times 10^{-7}$  and  $\alpha = 2.3 \times 10^{-4}$ ) defined using the method described in the previous section.

530 Figure A2 shows the fit to gravity data obtained after inversion with or without starting model, with  
 531 or without damping model regularization, and with or without cross-gradient constraints. Figure A3  
 532 shows the different density models obtained with the different types of inversions.

533 In Figures 8a-b and A3a-b, the case 1 is treated without or with a starting model. In the recon-  
 534 structed model, the strongest density anomalies concentrate close to the surface where the highest  
 535 gravity anomalies are present. This example illustrates that gravity inversion has a poor depth reso-  
 536 lution. However, a better reconstruction of density anomalies close to the surface is achieved when a  
 537 starting model is introduced (Figures A3c).

538 In case 2, densities are computed at depth with or without starting model and are exhibiting strong  
 539 similarities (see Figures A3d-e). The solution is very close to the one obtained in case 1 when a starting  
 540 model is introduced and no damping term is involved (see also Figure 8c). This result suggests that the  
 541 damping term acts as a depth-dependent preconditionner of the matrix system (A.1) but the starting  
 542 model does not prevent the inversion from concentrating the anomalies close to the surface.

543 In case 3 (Figure A3-f), the cross-gradient term adjusts the densities at depth to follow the varia-  
 544 tions of the  $V_p$  model. But, as it is the case here, if no physical Nafe-Drake scaled starting model or  
 545 if no damping term based on this prior model is introduced, these density variations are not following  
 546 successfully the  $V_p$  variations at depth, more specifically close to the crust-mantle transition (between  
 547 30 and 40 km depth). The inverted model obtained is smoothed too much everywhere in the compu-  
 548 tational domain. In Figure A4, an extreme case without data misfit minimization is considered while  
 549 keeping the cross-gradient term only in the total misfit cost function. We can observe that the data  
 550 distribution is reaching values closer to the real gravity data with a pronounced smoothing around the  
 551 highest anomaly values.

552 In summary, these different tests suggest that more physical inverted physical models can be ob-  
 553 tained during the inversion process by introducing a Nafe-Drake prior model as a starting model or  
 554 into the damping model term, or both, and by applying simultaneously the cross-gradient term in order  
 555 to distribute physically the density variations at depth, as can be seen in 8d-e. The simultaneous min-

556 imization of the gravity data misfit, the model damping regularization term and the cross-gradient is  
557 necessary. Now, in the next section, we show how the different terms of the cost function are behaving  
558 when optimal  $\lambda$  and  $\alpha$  are chosen.

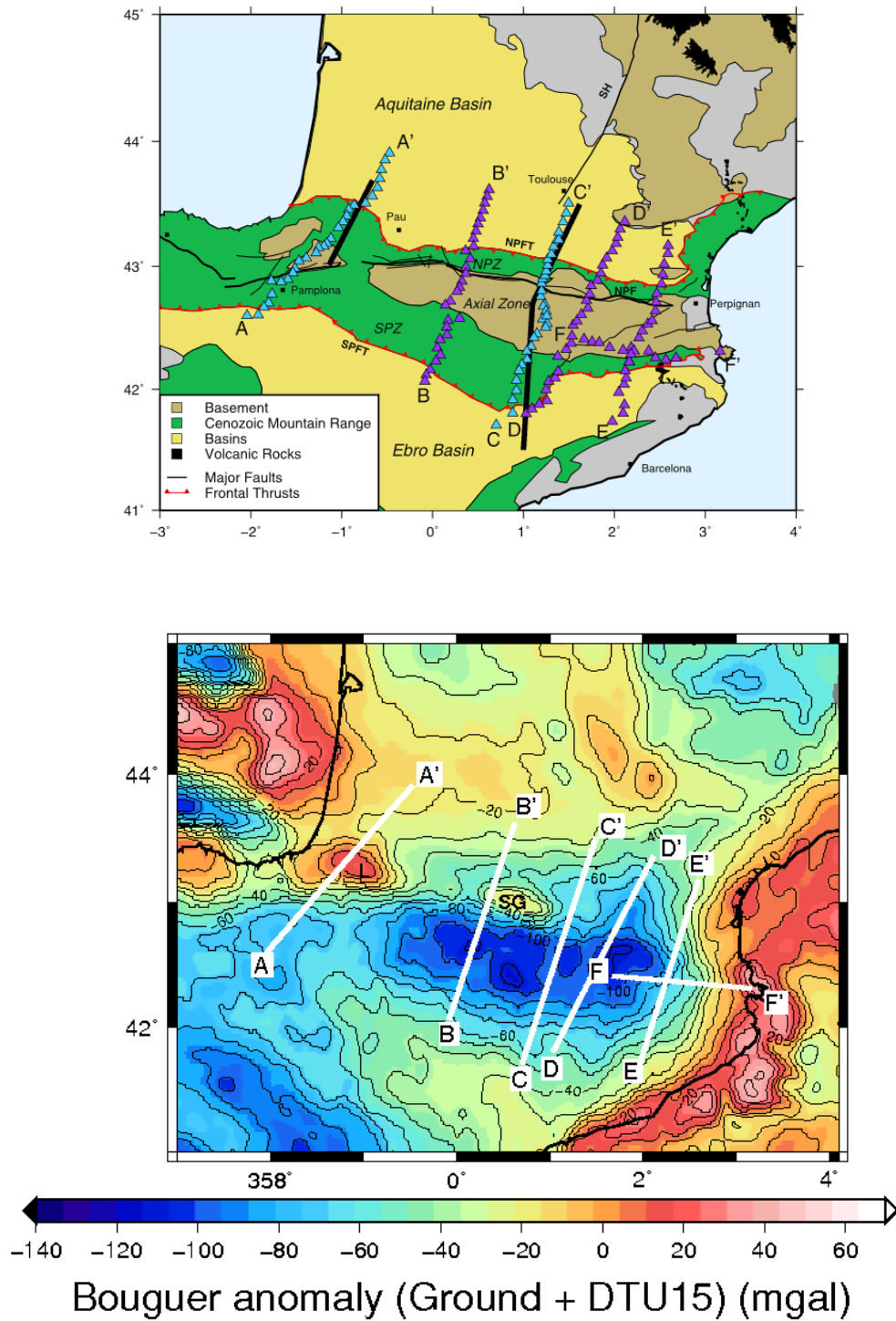


**Figure A1.** (Top) PYROPE and OROGEN seismic transects, and permanent seismic stations (Chevrot et al. 2018). The triangles represent the stations of the PYROPE (blue) and OROGEN seismic transects (purple). The thick black lines represent the ECORS-Pyrenees and ECORS-Arzacq deep seismic sounding profiles, located in the Central and Western Pyrenees. (Bottom) BGI gridded Bouguer anomaly data at 2 mn arc resolution in Southwest France and North Spain. Figure extracted from Chevrot et al. (2018)

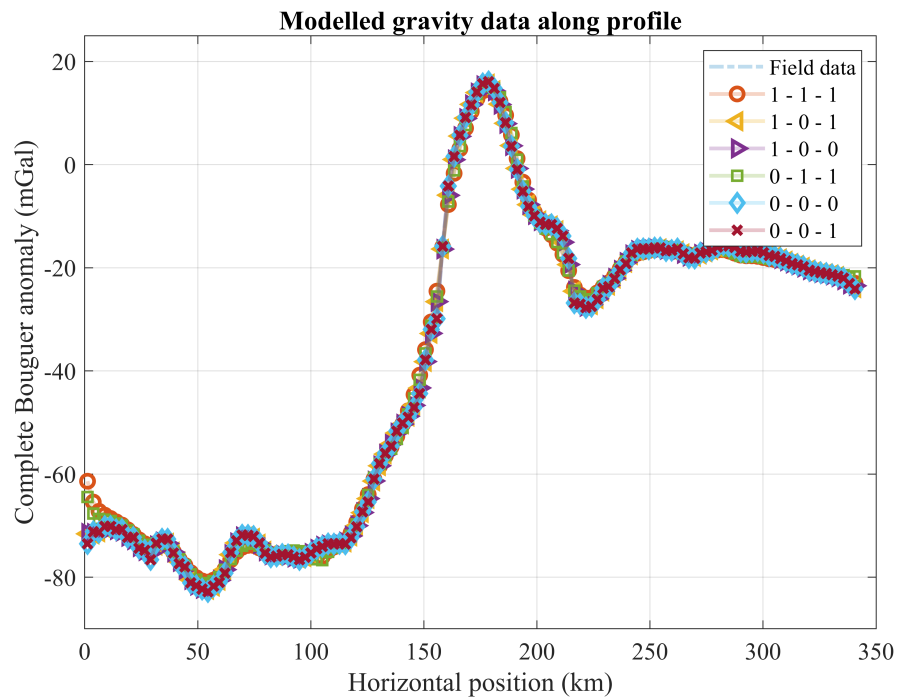


**Figure A2.** Observed and inverted gravity data with (1) or without (0) starting model, with or without model damping regularization, with or without cross-gradient constraint.

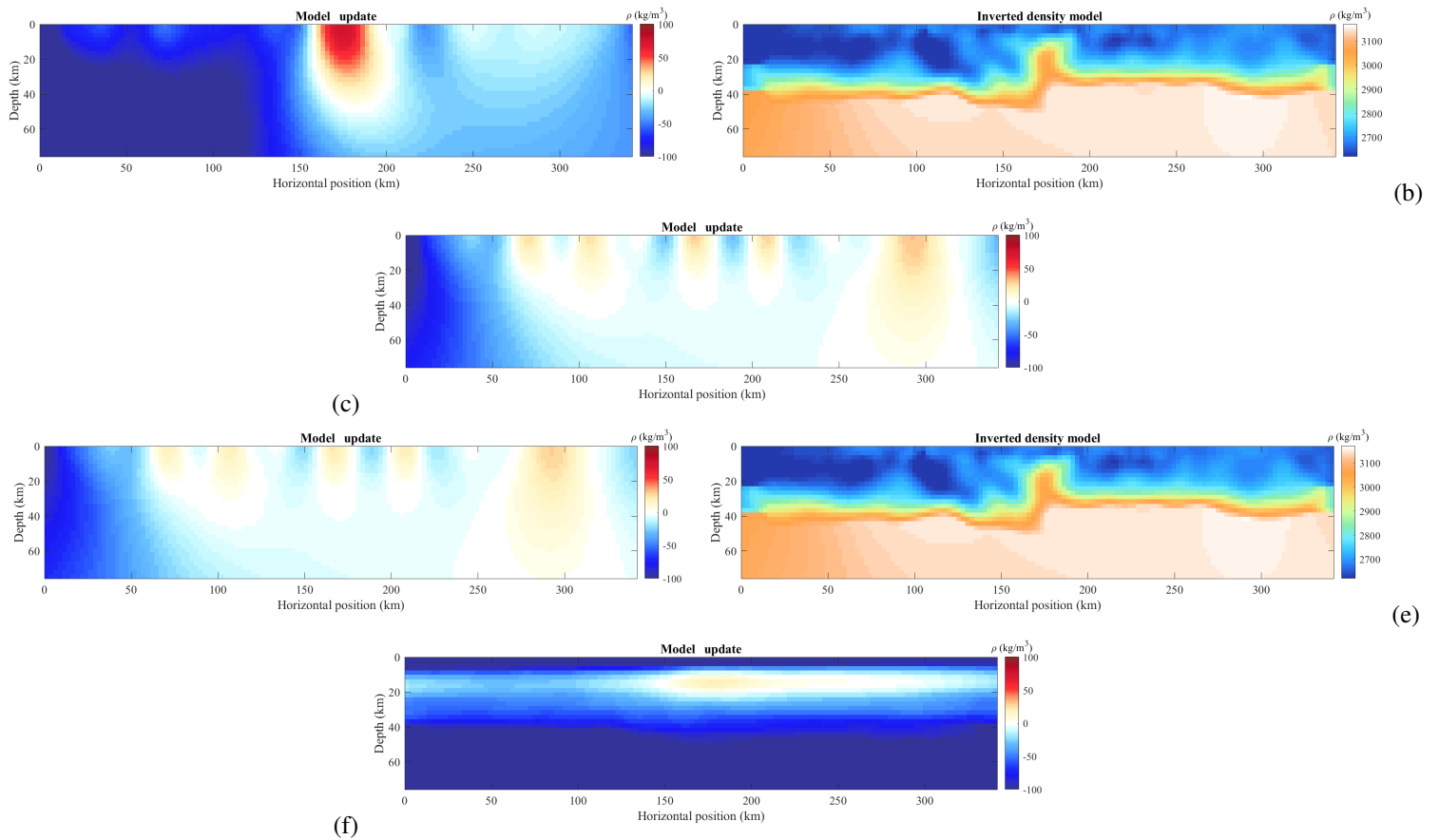


**Figure A3.** Results of inversions without any cross-gradient regularization (a to e) according to cases 1, 2 and 3.

**Case 1 :** Inverted anomalies (a) and effective densities (b) are obtained without damping on the model ( $\lambda = 0$ ), without starting model and without cross-gradient ( $\alpha = 0$ ). Solutions are locate close to the surface. In Figure (c), a starting model is introduced : anomalies appear close to the surface and at depth. **Case 2 :** In Figures (d) and (e), a damping regularization is applied on the model ( $\lambda \neq 0$ ) with a starting model as in figure (c) : similar anomalies appear close to the surface and at depth when compared to figure (c) but with slightly smaller values close to the surface. **Case 3 :** In figure (f), only cross-gradient regularization is applied ( $\alpha \neq 0$ ), without imposing a starting model and without model damping ( $\lambda = 0$ ) : the solution is not physical with too much smoothing at depth.

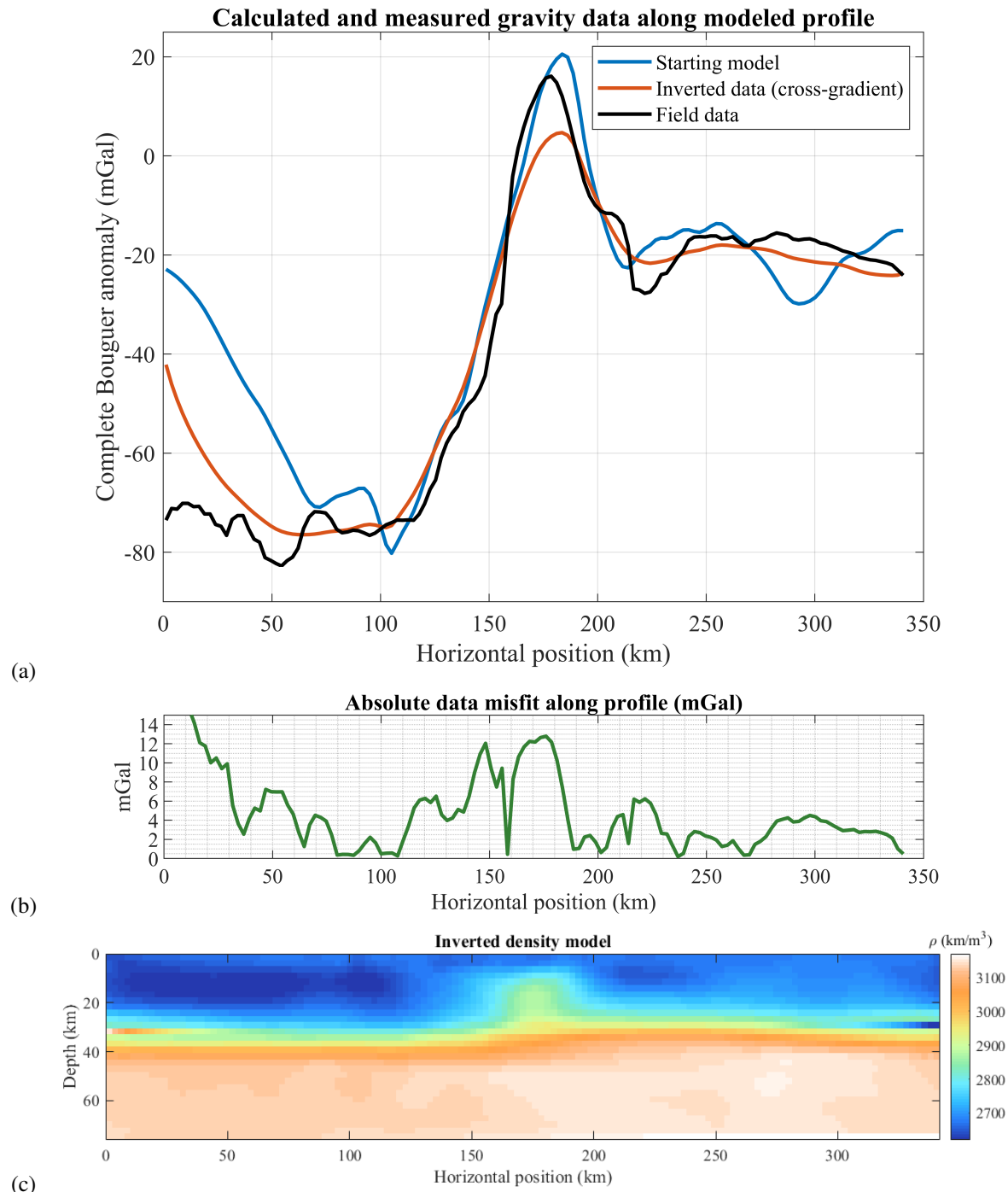
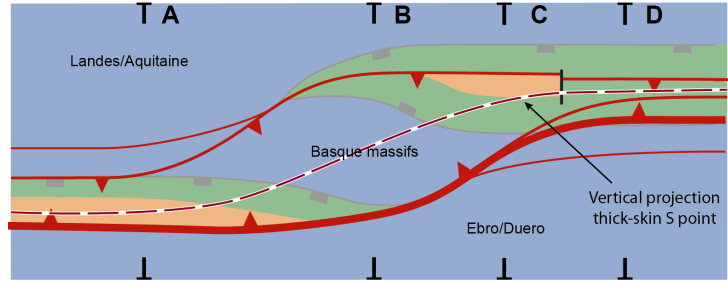
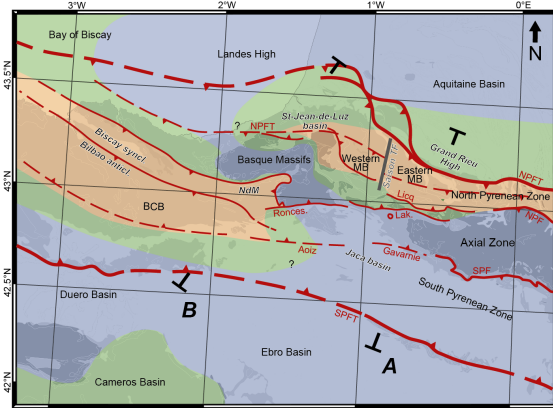


**Figure A4.** Gravity data and models obtained along the seismic profile in an extreme case after minimization of the cost function involving the cross-gradient function alone (no data misfit and no damping on the model, i.e.  $\lambda = 0$ , are considered) for the 2.5D case. (a-Top) Representation of the observed, prior and inverted Bouguer gravity data. (b-Middle) Data misfit between observed data and inverted data obtained after reaching a zero cross-gradient between density anomalies and  $V_p$  seismic velocities. (c-Bottom) Inverted densities respecting the zero cross-gradient condition. Too smooth models are recovered in this specific case.

Eocene to present-day

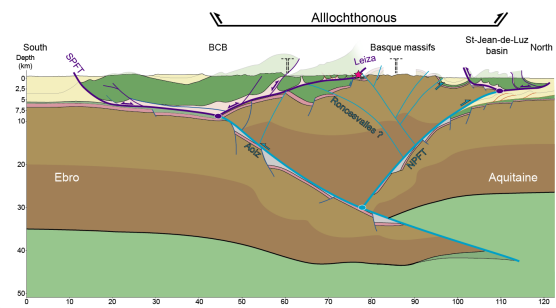
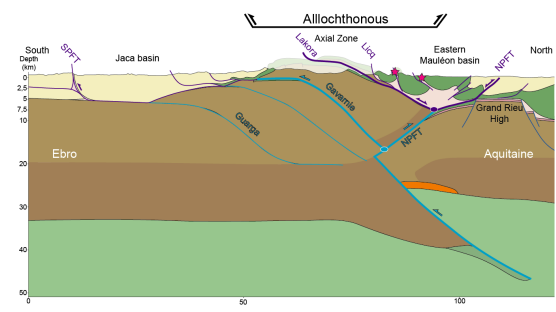
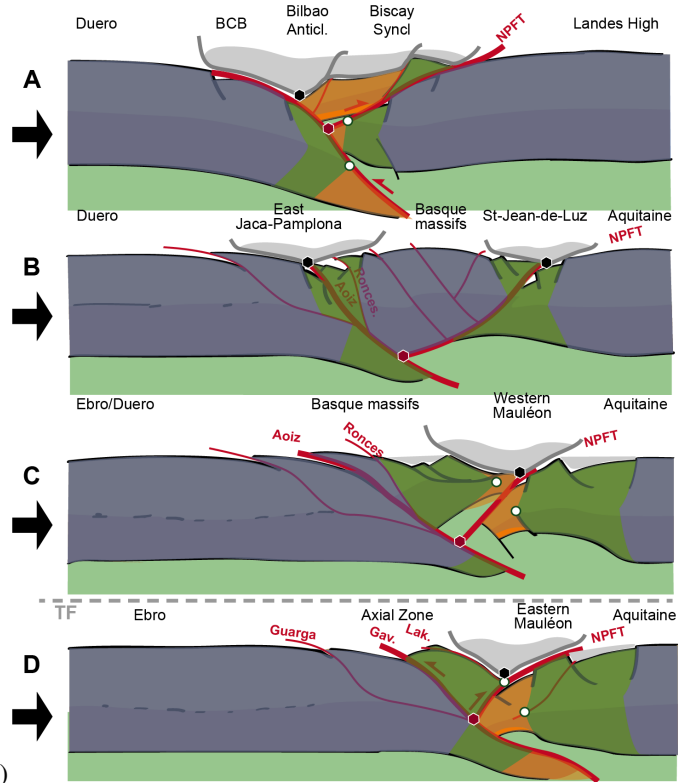


Present-day



Collisional stage

Cylindrical orogenic wedge formation



(A)

(B)

**Figure A5.** Collisional model proposed in the western Pyrenees for the Eocene to present day period by Lescoutre & Manatschal (2020), and coherent to the one proposed by Gómez-Romeu et al. (2019). Figure (A) : Southwest-northeast cross sections A and B passing through eastern and western Mauleon basin (chapter III, p. 121 of Lescoutre (2019)). Figure (B) : Cross section D passing through Eastern Mauleon (figure III-4, chapter III, p. 131 in Lescoutre (2019)) is very similar to our imaged A-A' section shown in Figure 14.